

UNIVERSITY OF GRONINGEN  
KAPTEYN ASTRONOMICAL INSTITUTE



ASTRONOMY

---

# Simulations and Measurements of a Reflective Polarization State Rotator

---

*Author:*  
Job Formsma  
S2758717

*Supervisor:*  
Dr. Ir. W. Jellema

March 30, 2020

## Abstract

A basic reflective resonant immersed half-wave plate was made and measured for its properties. First a generic model was developed using the transmission line theory that can model the reflectance, transmittance and absorption of multi-layered dielectric systems. The model was tested with lab samples, compared with results from the literature and showed good results. Measurements were done on the self-made plate to test its ability to rotate the polarization state of incident radiation. The data showed that more measurements and further improvements have to be made on the plate to get conclusive results. Despite this, the dielectric constant of RT/Duroid® 6002 could be measured between 84 GHz and 124 GHz and is  $3.04 \pm 0.03$ .

# Contents

<b>1</b>	<b>Introduction</b>	<b>2</b>
1.1	Fabry-Perot Interferometer	2
1.2	FIT Internship	2
1.3	Objectives	3
<b>2</b>	<b>Theory</b>	<b>4</b>
2.1	Fresnel Equations	4
2.2	Transmission Line Theory	6
2.3	Polarization State Representation	9
<b>3</b>	<b>Multi-Layer Model</b>	<b>12</b>
3.1	Description	12
3.2	Validation	12
3.2.1	Fresnel Equations	12
3.2.2	Other Models	14
3.2.3	Anti Reflection Coating	14
<b>4</b>	<b>Reflective Half-Wave Plate</b>	<b>17</b>
4.1	Purpose	17
4.2	Modeling	19
4.2.1	Phase Shift	19
4.2.2	Polarization State Rotation	20
4.3	Fabrication	22
4.3.1	Dielectric Material	22
4.3.2	Polarizing Wire Grid	22
4.3.3	Ground Plate	24
4.4	Simulations	24
<b>5</b>	<b>Experimental Set-up</b>	<b>26</b>
5.1	Devices	26
5.2	Automation	27
5.3	Transmission Setup	27
5.4	Reflection Setup	28
<b>6</b>	<b>Data Analysis</b>	<b>30</b>
6.1	Transmission Tests	30
6.1.1	HDPE	30
6.1.2	Fabry-Perot etalon	32
6.1.3	RT/duroid	32
6.2	Reflection Tests	34
6.2.1	$s$ -polarization	35
6.2.2	$p$ -polarization	36
<b>7</b>	<b>Discussion</b>	<b>37</b>
<b>8</b>	<b>Summary and Conclusions</b>	<b>40</b>

# 1 Introduction

A wide variety of interference techniques are used in Astronomy. Large telescope arrays observe the radio sky by combining signals from multiple telescopes. Optical systems are tested using wave front sensing techniques to check if a light beam propagates correctly through the system. In this project another form of interference is used, namely the interference due to reflections inside a dielectric material. This interference is realized in a Fabry-Perot etalon and is widely used in optical engineering in the field of multi-layer thin film coatings. Applications include: anti-reflection coatings, dichroic filters, beamsplitters, bandpass filters and more. In this project the concept of interference inside dielectric materials will be used to model and assemble a simple reflective half-wave plate.

## 1.1 Fabry-Perot Interferometer

A Fabry-Perot interferometer consists of two parallel surfaces or mirrors which create an optical cavity. Incident light resonates between the surfaces and will only pass through the system if the light is in resonance. The resonances depend on the distance between the mirrors and the frequency of the incident light. By tuning the distance between the mirrors the Fabry-Perot can be set to a specific resonance frequency. This creates a band-pass filter to a set of frequencies and can be used to probe a specific emission line.

The simplest Fabry-Perot interferometer (or *etalon*) is a slab of dielectric material. As radiation passes through the material it goes through two distinctive interfaces: the surface passing into the material and the surface passing out of the material. These act as two parallel surfaces, where internal reflections create an optical cavity. Multiple dielectric slabs can be put together in a system resulting in more resonance cavities and reflections. These multi-layered systems can be tuned to create an even more narrow band-pass filter.

During the projects of Carolien Feenstra, see [Feenstra, 2017] and [Feenstra, 2019], the feasibility of a multi-layered Silicon Fabry-Perot was examined to use as a spectrometer for astronomical missions in the THz or far-infrared wavelength regime. The research focused on losses in dielectric materials, modeling, and designing a prototype.

## 1.2 FIT Internship

This project is part of the *Fysische Informatie Techniek* (FIT) internship course of the University of Groningen. It is focused on making students familiar with the aspects of information technology and the control of physical processes. Projects in this internship also include using information technical aspects, such as: programming, design, construction and testing. In contrary to a BSc or MSc research, the FIT internship is not only about scientific research, but is also about working in a scientific research environment. Apart from conducting research, it is important to learn to work in a group, continue the work of others and work with experimental physics. All these concepts are touched upon during this project and the related practical work is highlighted in the next section.

### 1.3 Objectives

The original goal of this internship was to repeat the measurements performed in [Feenstra, 2019] at different wavelengths to determine the feasibility of the SRON<sup>1</sup> Fabry-Perot Etalon for astronomical observations. However, due to global shortage of helium during the project this was not possible. We moved away from the Fabry-Perot etalon measurements and came up with different goals still based on the theory and work described in [Feenstra, 2019].

The project composes of building an experimental setup, measure a self-made device and develop a model which can be used to explain the outcomes. First a generic model will be made which can simulate the response of incident light on multi-layered dielectric systems. The model will be tested by measuring different lab samples in an experimental setup. The setup will be fully automated using Python, to make measuring more convenient during this project and for future measurements of the SRON Fabry-Perot etalon. The setup will be run with a single script which automatically starts a measurement, stores data and safely shuts down the setup. We will model and also fabricate a reflective half-wave plate which can be used to rotate the polarization state of incident electromagnetic radiation. The plate will be tested using the automated setup and the model is used to explain the results.

The theory used to model multi-layer dielectric systems is described in section 2. Two different approaches are described to understand the interference in such a system. The approaches are used to develop a generic model which is discussed in section 3, along with test cases for validation of the model. Fabrication of the experimental sample is described in section 4 and the automated setup to test the sample in section 5. Measurements of the sample and data analysis on the outcomes can be found in section 6. The results are discussed in section 7 and conclusions of this project are made in section 8.

---

<sup>1</sup>SRON Netherlands Institute for Space Research, Groningen

## 2 Theory

The reflectance and transmittance of light propagating through a multi-layered system, such as the SRON Fabry-Perot etalon, can be described by two different methods. The first method uses the Fresnel equations and can describe the interaction of light between two mediums [Hecht, 2002]. At the interface between the two mediums, the light will reflect and refract due to difference in refractive index. This interaction can be described by the Fresnel equations and can be used to determine the ratio of reflectance and transmittance. The second method uses the transmission line theory in which we consider the light, or electromagnetic waves, as a voltage inducing currents in an electrical circuit that represents dielectric layers [Goldsmith, 1998]. By looking at the impedance of the layers in the system the reflectance and transmittance can be calculated.

For multi-layered systems the derivations from the Fresnel equations become very complex as all reflections in and between layers have to be tracked individually. This implies that in most practical situations the Fresnel equations can only be used for simple single layer systems. The transmission line theory is a more general approach which can be used to model and stack the individual layers in a system. The general theory can describe the response of any multi-layered dielectric system with an arbitrary amount of layers and will eventually be used in our model.

### 2.1 Fresnel Equations

The simplest Fabry-Perot etalon is a single slab of dielectric material surrounded by air. Light that propagates through the slab goes through two interfaces: into the medium and out of the medium. At these interfaces the refractive index of the propagating medium changes and the light will reflect or refract according to the Fresnel equations. At a single interface the boundary conditions are described by the law of reflection and the law of refraction. The incident, reflected and refracted angles of the propagating radiation relate by

$$\theta_i = \theta_r , \quad (1)$$

$$n_i \sin \theta_i = n_t \sin \theta_t . \quad (2)$$

with  $\theta_i$  the angle of incidence,  $\theta_r$  the angle of reflection and  $\theta_t$  the angle of the transmitted (or refracted) radiation. The refractive index of the materials is denoted with  $n_i$  and  $n_t$ . The refractive index of a dielectric material can be related to its relative permittivity via

$$n = \sqrt{\tilde{\epsilon}} , \quad (3)$$

where the dielectric constant  $\tilde{\epsilon}$  is composed of a real and complex components as in

$$\tilde{\epsilon} = \epsilon' + i\epsilon'' . \quad (4)$$

The dielectric loss  $\delta$  of a dielectric material quantifies the ability to dissipate radiation inside the material into heat. The absorption parameter *loss tangent*, that is used in this project, is defined as the ratio of the imaginary and real components of the dielectric constant

$$\tan \delta = \frac{\epsilon''}{\epsilon'} . \quad (5)$$

The electric field components of the radiation is also conserved. The tangential component of the electric field is continuous at the interfaces described by

$$\mathbf{E}_i + \mathbf{E}_r = \mathbf{E}_t . \quad (6)$$

The Fresnel equations describe the reflection and transmission coefficient of the incident light propagating through the system. The coefficients are described by

$$r = \frac{\mathbf{E}_r}{\mathbf{E}_i} \quad \text{and} \quad t = \frac{\mathbf{E}_t}{\mathbf{E}_i} , \quad (7)$$

where the reflection coefficient  $r$  is the ratio of reflected radiation over the incident radiation and the transmission coefficient  $t$  the ratio of transmitted radiation over the incident radiation. The full definitions are shown in Appendix A. The reflection and transmission coefficients are used to determine the real reflectance and transmittance of the interface, which are the squared magnitudes of the coefficients.

$$\mathcal{R} = |r|^2 \quad \text{and} \quad \mathcal{T} = \frac{n_t \cos \theta_t}{n_i \cos \theta_i} |t|^2 . \quad (8)$$

Note that the transmittance has an extra component, describing the distribution of energy transported into and out of an interface dependent on the refractive index of the different materials. The reflectance and transmittance equations (8) only hold for a single interface, but a slab has two interfaces. As light transmits through the first interface, it reflects off the material and will also enter the slab. Inside the material there can be internal reflections from the second interface back to the first interface. Again, there can be an internal reflection resulting in a cascade of back and forth reflections. This is best visualized in Figure 1, where the internal reflections are shown in the dielectric slab.

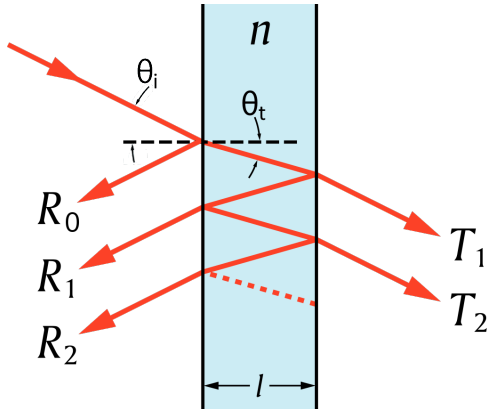


**Figure 1:** Fabry-Perot etalon. Light enters and undergoes multiple internal reflections. Work by Kevin J. Morse.

The path length in the slab varies with the angle of incidence  $\theta_i$  and the thickness  $l$  of the slab. The reflected and transmitted light leaves the slab at different phases due to the path differences, resulting in interference between the rays. If we vary the thickness of the slab or the angle of the incident radiation we can tune the phase differences and tune the amount of interference. By tuning these parameters there can be constructive and destructive interference, resulting in a Fabry-Perot device in which light of specific frequencies is either fully reflected or transmitted.

The cascade of internal reflections are calculated by [Feenstra, 2017] and is briefly described in Appendix A to give the reader an idea of complexity.

## 2.2 Transmission Line Theory

To describe the propagation of light through a system, such as a Fabry-Perot etalon, we can also use the transmission line theory. A transmission line is a cable or structure in an electric circuit that conducts alternating current in the radio frequency regime, like a cable for television signals. This theory can also be applied to the general case of electromagnetic waves propagating through a dielectric medium. We will use this theory to describe the conducting properties of a system and derive the equations which describe how the light will propagate. This method is more applied to the physical properties of the system, rather than using Fresnel equations on the propagation of electromagnetic waves through different materials.

To eventually describe the transmission line theory we first have to understand the concept of impedance. The impedance ( $Z$ ) of a medium is the opposition of forming a current when a voltage is applied. For a dielectric medium the impedance is dependent on its dielectric constant. As the Fabry-Perot etalon is surrounded by air, the electromagnetic waves propagate through different mediums with different impedances.

The zero impedance of free space (air) is given as

$$Z_0 = \sqrt{\frac{\mu_0}{\epsilon_0}} \approx 120\pi \Omega . \quad (9)$$

The free space impedance is used to determine the impedance of the incident beam on the Fabry-Perot etalon and also the impedance of the etalon itself. The source impedance  $Z_s$  of the incident radiation is dependent on polarization relative to the slab and is:

$$Z_{s\parallel} = Z_0 \cos \theta_i \quad \text{and} \quad Z_{s\perp} = \frac{Z_0}{\cos \theta_i} , \quad (10)$$

where  $\theta_i$  is the angle of incidence of the beam on the normal of the etalon. The load impedance  $Z_l$  of a dielectric slab with dielectric constant  $\epsilon$  can be derived by applying Snell's Law and rewriting to

$$Z_{l\parallel} = \frac{Z_0 \sqrt{\epsilon - \sin^2 \theta_i}}{\epsilon} \quad \text{and} \quad Z_{l\perp} = \frac{Z_0}{\sqrt{\epsilon - \sin^2 \theta_i}} . \quad (11)$$

As the impedance is dependent on the dielectric constant of the medium, the propagating electromagnetic waves go through multiple interfaces at which the impedance changes. This change in impedance results in reflections.

The impedance of a dielectric material is equivalent to the resistance of an electric circuit. The impedance is described by the ratio of the electromagnetic field  $\mathbf{E}$  and the induced magnetic field  $\mathbf{H}$ , whereas the resistance in an electric circuit can be described by the ratio of the voltage  $V$  and the current  $I$ . This correspondence gives that the response of dielectric layers can be described by the response of transmission line circuits.

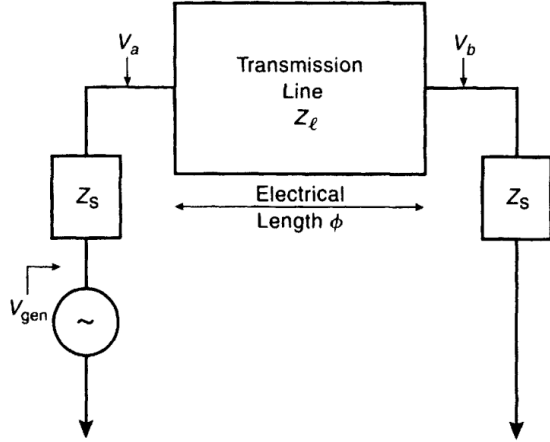


**Figure 2:** Transmission line circuit equivalent of a slab of dielectric material [Goldsmith, 1998]

In Figure 2 the transmission line circuit is given which is equivalent to radiation propagating through a slab of dielectric material. Instead of radiation passing through a medium we have an input voltage and current passing through an electric circuit. The voltage and current along the transmission line can be described, as:

$$V(z) = e^{-ikz} - \rho e^{ikz} \quad \text{and} \quad I(z) = \frac{e^{-ikz} + \rho e^{ikz}}{Z_l}, \quad (12)$$

where  $\rho$  is the ratio of waves traveling in reverse due to reflections at the interfaces, just as light reflecting off a surface. The voltage and current at the beginning of the transmission line and at the end of the transmission line can be derived by substitution into (12). At the input (left of the transmission line in Figure 2) with  $z = 0$  we have:

$$V_a = 1 - \rho \quad \text{and} \quad I_a = \frac{1 + \rho}{Z_l}, \quad (13)$$

while for the output with  $kz = \phi$  we have:

$$V_b = e^{-i\phi} - \rho e^{i\phi} \quad \text{and} \quad I_b = \frac{e^{-i\phi} + \rho e^{i\phi}}{Z_l}. \quad (14)$$

As the impedance is the opposition of creating a current when a voltage is applied, we can set the ratio of the voltage over the current  $V_b/I_b$  at the output of the transmission line to be the source impedance. This is allowed as the voltage  $V_b$  induces a current described by  $I_b$ . By rewriting the transmission line voltages we can determine the ratio of reverse waves  $\rho$  in the transmission line to be

$$\rho = r e^{-2i\phi}, \quad (15)$$

with

$$r = \frac{Z_l - Z_s}{Z_l + Z_s}, \quad (16)$$

where  $Z_s$  is the source impedance as shown in Figure 2. Equation (16) is the reflection coefficient for an infinite long transmission line which represents a single reflection on a Fresnel surface.

Up to now we only considered an unit voltage as input. Looking at Figure 2 we see that the input voltage can be given by  $V_{\text{gen}}$ , from which we can compute the reflection and transmission coefficients using all the theory described above.

This derivation is shown in Appendix B and yields the following equations for the transmission line reflection and transmission coefficients:

$$r_{\text{tl}} = \frac{-2ir \sin \phi e^{-i\phi}}{1 - r^2 e^{-2i\phi}} \quad \text{and} \quad t_{\text{tl}} = \frac{(1 - r^2)e^{-i\phi}}{1 - r^2 e^{-2i\phi}}. \quad (17)$$

The transmission coefficients obtained look similar to the transmission coefficients found by the Fresnel derivation (Eq. (48)). Above theory gives an impression about how the transmission line theory works for a single slab of dielectric material. We will now expand to a multi-layer version of the transmission line theory, to be able to describe a Fabry-Perot etalon consisting of multiple layers. This gives significant better resolution and response on incident radiation.

We expand on the transmission line circuit by describing it via a transmission line matrix. Instead of using (12), (13) and (14) to determine the reflections, the system is described by a matrix which relates the input voltage and current to the output of the system. This is described as:

$$\begin{bmatrix} V_{\text{in}} \\ I_{\text{in}} \end{bmatrix} = \begin{bmatrix} A & B \\ C & D \end{bmatrix} \begin{bmatrix} V_{\text{out}} \\ I_{\text{out}} \end{bmatrix}, \quad (18)$$

where the  $ABCD$  matrix contains the information such as the impedance of the system. This can be related to electromagnetic radiation propagating through a single layer of dielectric material. The elements  $A$  and  $D$  are dimensionless,  $B$  is in units of impedance and  $C$  is in units of admittance. For a Fabry-Perot system in free space, the input impedance is the same as the output impedance. This yields the relationship of

$$Z_l = \frac{AZ_s + B}{CZ_s + D}. \quad (19)$$

Using a similar strategy as described in Appendix B, the reflection and transmission coefficients can be derived as:

$$r = \frac{AZ_s + B - CZ_s^2 - DZ_s}{AZ_s + B + CZ_s^2 + DZ_s}, \quad (20)$$

$$t = \frac{2Z_s}{AZ_s + B + CZ_s^2 + DZ_s}. \quad (21)$$

The total reflectance and transmittance are found in a similar way as shown in (8). The reflectance is the squared magnitude of the reflection coefficient and the transmittance is the squared magnitude of the transmission coefficient times the ratio of the impedance of the input medium and the output medium. In our example the input medium and output medium both have the same impedance  $Z_s$ , which gives a multiplication by 1.

The matrix elements are defined as

$$A = \cosh \gamma d, \quad B = Z_l \sinh \gamma d, \quad C = \frac{1}{Z_l} \sinh \gamma d, \quad D = \cosh \gamma d, \quad (22)$$

where  $Z_l$  is the load impedance of the medium,  $d$  the thickness of the layer and  $\gamma$  is defined as

$$\gamma = i \left( \frac{2\pi n}{\lambda_0} \right) \cos \theta_t, \quad (23)$$

where  $n$  is the refractive index of the medium,  $\lambda_0$  the wavelength of the incident radiation in free space and  $\theta_t$  the transverse angle in the medium. The matrix method is useful because it can be used on multiple layers. If multiple layers are put together, then the individual  $ABCD$  matrices can be multiplied to get a single  $ABCD$  matrix which describes the full system. This gives that equation (18) becomes

$$\begin{bmatrix} V_{\text{in}} \\ I_{\text{in}} \end{bmatrix} = \begin{bmatrix} A_1 & B_1 \\ C_1 & D_1 \end{bmatrix} \begin{bmatrix} A_2 & B_2 \\ C_2 & D_2 \end{bmatrix} \cdots \begin{bmatrix} A_n & B_n \\ C_n & D_n \end{bmatrix} \begin{bmatrix} V_{\text{out}} \\ I_{\text{out}} \end{bmatrix}, \quad (24)$$

for  $n$  layers in the system. By multiplying the matrices we get (18) and can apply the full theory as if it were a single layer. The transmission line also works for absorption in the medium by inputting a complex dielectric constant.

The transmission line matrix is also used for special layers in the system, such as a shunt element or a wire grid. In contrary to the dielectric layers we described up to now, these layers can be made up of thin films of metal or metal-based patterns. The transmission line theory is therefore very suitable for devices composed of dielectric layers as well as metal layer optics. The elements of the  $ABCD$  matrix for a shunt element consist mostly of fixed values

$$A = 1, \quad B = 0, \quad C = 1/Z_g, \quad D = 1, \quad (25)$$

For a shunt element or mirror,  $Z_g$  is simply the surface impedance or the surface resistance of the layer. The surface impedance of a grid element is dependent on the shape of the wire grids and their dimensions. For the incident electric field parallel to the direction of the grid strips, the surface impedance in the long-wavelength limit for a grid of strips is [Goldsmith, 1998]:

$$Z_g = i Z_0 \left( \frac{g}{\lambda} \right) \ln \csc \left( \frac{\pi a}{g} \right), \quad (26)$$

where  $g$  is the strip period and  $2a$  the strip width.

### 2.3 Polarization State Representation

Dielectric layers change the polarization state of the incident radiation when it is under a non-zero angle. This is due to the differences between the impedance for  $s$ -polarized and  $p$ -polarized light. To describe the polarization state changes we can apply the theory of Jones matrices [Hecht, 2002]. Polarized light can be represented as a Jones vector and components in the system as Jones matrices. When the light propagates through a component, the polarization state change can be described by the product of the Jones vector and the Jones matrix. Just as the transmission line theory, the Jones calculus can be applied on a series of elements via matrix multiplication.

Suppose a light beam polarized in an arbitrary direction encounters a wire grid rotated at an arbitrary angle as shown in the left picture of Figure 3. Part of the light will be reflected due to the grid wires and part of the light will transmit through the grid. To compute these values we define two coordinate systems: a global coordinate system  $(\hat{x}, \hat{y})$  and a local coordinate system  $(\hat{x}', \hat{y}')$  where  $\hat{y}'$  is parallel to the grid wires. Then the mapping of the Jones vector of the incident electric field is

$$\begin{bmatrix} E_{x'} \\ E_{y'} \end{bmatrix} = \bar{R} \begin{bmatrix} E_x \\ E_y \end{bmatrix}, \quad (27)$$

with  $\bar{R}$  the rotation matrix for counter-clockwise rotation

$$\bar{R} = \begin{bmatrix} \cos \alpha & \sin \alpha \\ -\sin \alpha & \cos \alpha \end{bmatrix}. \quad (28)$$

The electric field components in the  $(\hat{x}', \hat{y}')$  coordinate system align nicely with the wires of the grid. For each component we can look at the response of an ideal grid. Parallel along the wires results in a reflection coefficient  $r = 1$  and transmission coefficient  $t = 0$ . Perpendicular of the wires gives opposite values:

$$E_{x'} \text{ is } \perp \text{ to grid} \rightarrow \quad t_s = 1, \quad r_s = 0 \quad (29)$$

$$E_{y'} \text{ is } \parallel \text{ to grid} \rightarrow \quad t_p = 0, \quad r_p = 1 \quad (30)$$

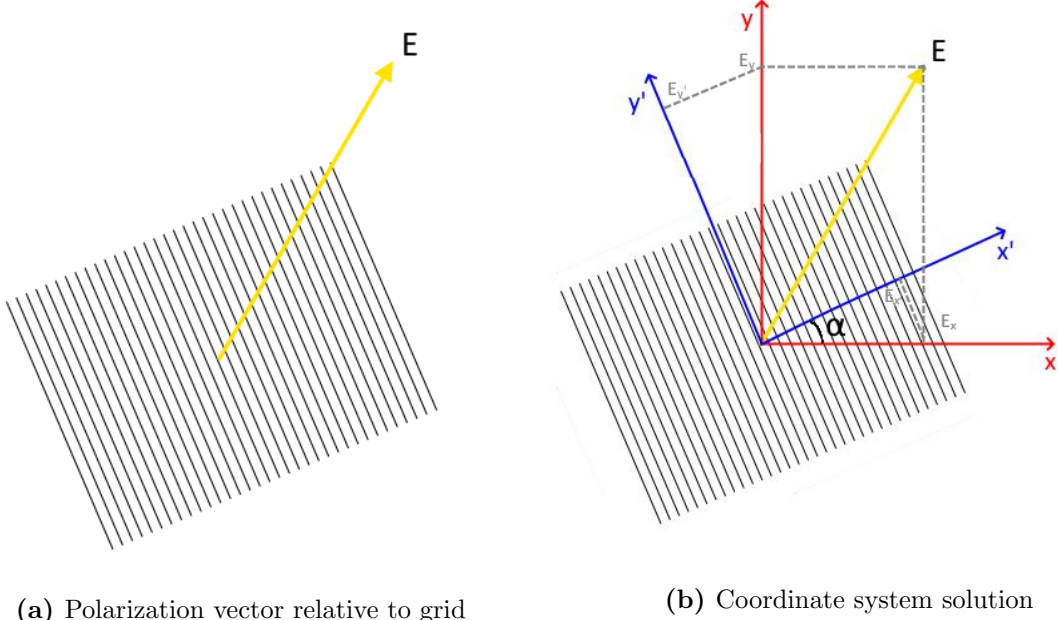


**Figure 3:** Incident radiation on a wire grid

These values allow us to define the Jones matrices of the grid. The vector along the  $\hat{x}'$  axis gives the transmitted part and along the  $\hat{y}'$  axis the reflected part. This gives the Jones matrices of the ideal grid to be

$$M_{t,\text{grid}} = \begin{bmatrix} t_s & 0 \\ 0 & t_p \end{bmatrix} = \begin{bmatrix} 1 & 0 \\ 0 & 0 \end{bmatrix} \quad \text{and} \quad M_{r,\text{grid}} = \begin{bmatrix} r_s & 0 \\ 0 & r_p \end{bmatrix} = \begin{bmatrix} 0 & 0 \\ 0 & 1 \end{bmatrix}. \quad (31)$$

The output electric field vectors are calculated by the product of the Jones vector and the Jones matrix of the ideal grid:

$$\vec{E}_{t,\text{out}} = \bar{R}^{-1} \bar{M}_{t,\text{grid}} \bar{R} \vec{E}_{\text{in}}, \quad (32)$$

$$\vec{E}_{r,\text{out}} = \bar{R}^{-1} \bar{M}_{r,\text{grid}} \bar{R} \vec{E}_{\text{in}}, \quad (33)$$

where the input vector is first rotated to the local coordinate system of the grid, then the response of the grid is calculated and lastly the vector is rotated back to the global coordinate system. For  $n$  wire grids under different rotations the response is calculated in a similar way as the  $ABCD$  matrix in the transmission line theory. The output vectors are given by

$$\vec{E}_{t,\text{out}} = (\bar{R}_n^{-1} \bar{M}_{t,\text{grid}} \bar{R}_n) \cdots (\bar{R}_2^{-1} \bar{M}_{t,\text{grid}} \bar{R}_2) (\bar{R}_1^{-1} \bar{M}_{t,\text{grid}} \bar{R}_1) \vec{E}_{\text{in}}, \quad (34)$$

$$\vec{E}_{r,\text{out}} = (\bar{R}_n^{-1} \bar{M}_{r,\text{grid}} \bar{R}_n) \cdots (\bar{R}_2^{-1} \bar{M}_{r,\text{grid}} \bar{R}_2) (\bar{R}_1^{-1} \bar{M}_{r,\text{grid}} \bar{R}_1) \vec{E}_{\text{in}}, \quad (35)$$

where for the different rotations we have the rotation matrices

$$\bar{R}_i = \begin{bmatrix} \cos \alpha_i & \sin \alpha_i \\ -\sin \alpha_i & \cos \alpha_i \end{bmatrix}. \quad (36)$$

In the experimental measurements of this project we have to keep track of the polarization state changes of the radiation due to grids and beamsplitters. These objects and the device under test can all be modelled using the transmission line theory. The transmission line theory calculates the reflection and transmission coefficients individually, so these field coefficients can be used in the Jones theory.

Instead of using the ideal grid with the coefficients shown in (31), the reflection and transmission coefficients derived by the transmission line theory can be used ((20) and (21)). This combines both theories and can thus be used to model a full measurement system that could consist of numerous devices like polarization grids, beamsplitters and multi-layered devices.

### 3 Multi-Layer Model

The reflectance and transmittance of a multi-layered device has to be simulated before a test sample can be made. We used the transmission line theory to develop a generic model<sup>2</sup> which can determine the reflectance, transmittance and absorption of multi-layered systems consisting of slabs of dielectric material with a given size.

#### 3.1 Description

The model can show the reflectance, transmittance and absorption of any multi-layered system with parametric inputs for frequency, angle of incidence, layer thickness, (complex) dielectric constant and polarization. It is written in Python based on an Object Oriented Programming methodology. The multi-layered system is defined as a class and handles the transmission line matrices as objects to construct the transmission line matrix of the full system.

The program files are complemented with documentation describing the input and output of the model. First, the system is build up by adding each individual layer. The reflectance and transmittance of this system is calculated after the parameters for the incident radiation are passed. The model is generic, as in, it can describe the reflectance and transmittance of different objects such as: cryostat windows, anti-reflection coatings and beamsplitters.

The system and radiation parameters are entered using either a text file or by using the public functions of the `System` class directly. When the layer and radiation information is inputted the individual  $ABCD$  matrices will be made of all the layers and the final system matrix will be calculated. The reflectance and transmittance is returned from the `System` object to the main file and can be plotted.

#### 3.2 Validation

It is important that the outcome of the model can be trusted. To test the Multi-Layer Model (*MLModel*) we compare it with the classic Fresnel equations. This method is used for simple single layer systems. If the outcome is similar, the *MLModel* can also be assumed to be correct for multi-layered systems, as the calculation of a single layer is the same as for multiple layers. An additional validation test is done by comparing a theoretical ideal anti-reflection coating with outcomes in the literature. Eventually the model is used on fitting data from experiments and is also cross-checked with a similar model by [Kozlova, 2019].

##### 3.2.1 Fresnel Equations

Simple single layer systems can be modelled with the Fresnel equations as described in section 2.1. The reflectance and transmittance calculated from these equations can be compared with a single layer input into the *MLModel*. This tests the accuracy of the *MLModel* and also confirms if the transmission line theory can be used for this application. The first test is computing the reflectance of a slab of Silicon. The thickness of the slab is set to 8 mm with a dielectric constant of 11.66 [Feenstra, 2017]. In Figure 4 and 5 we see that the output of the two methods overlap nicely. The difference is also shown, where due to low the values at the level of numerical noise we can conclude that there is no difference between the two methods.

---

<sup>2</sup>code: <https://github.com/Formsma/MLModel>

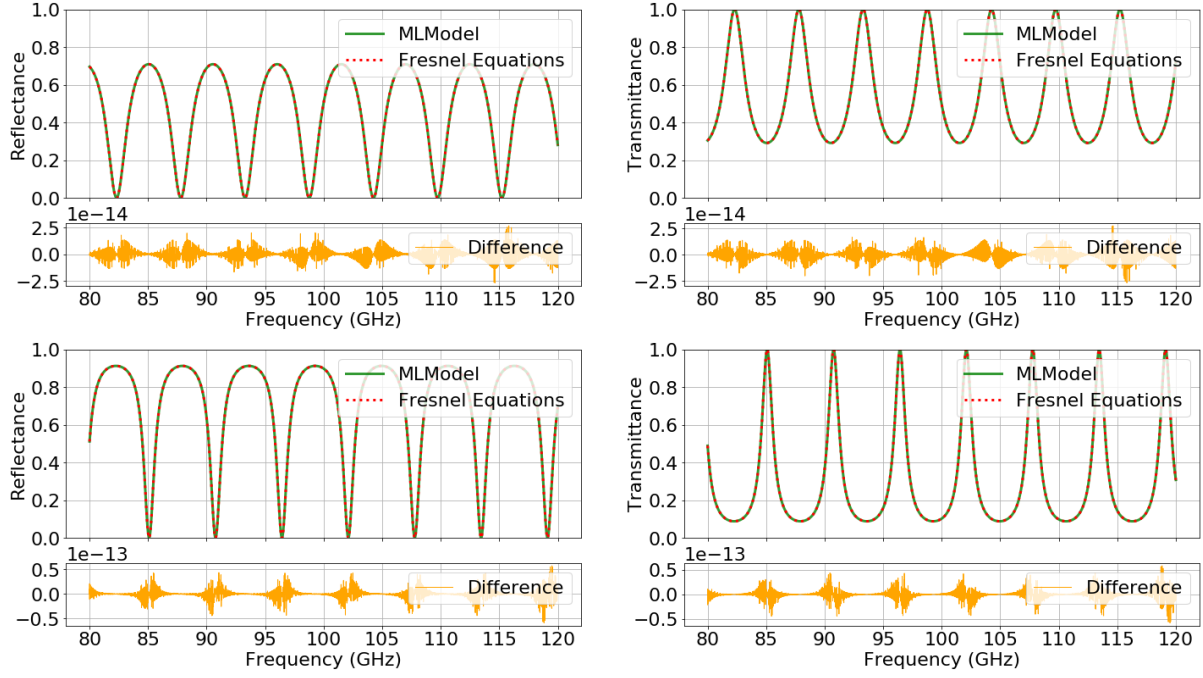


**Figure 4:** Comparison between Fresnel equations and the *MLModel* for s-polarized light. Top row is under a zero angle of incidence and the bottom row is under an angle of 60 degrees.

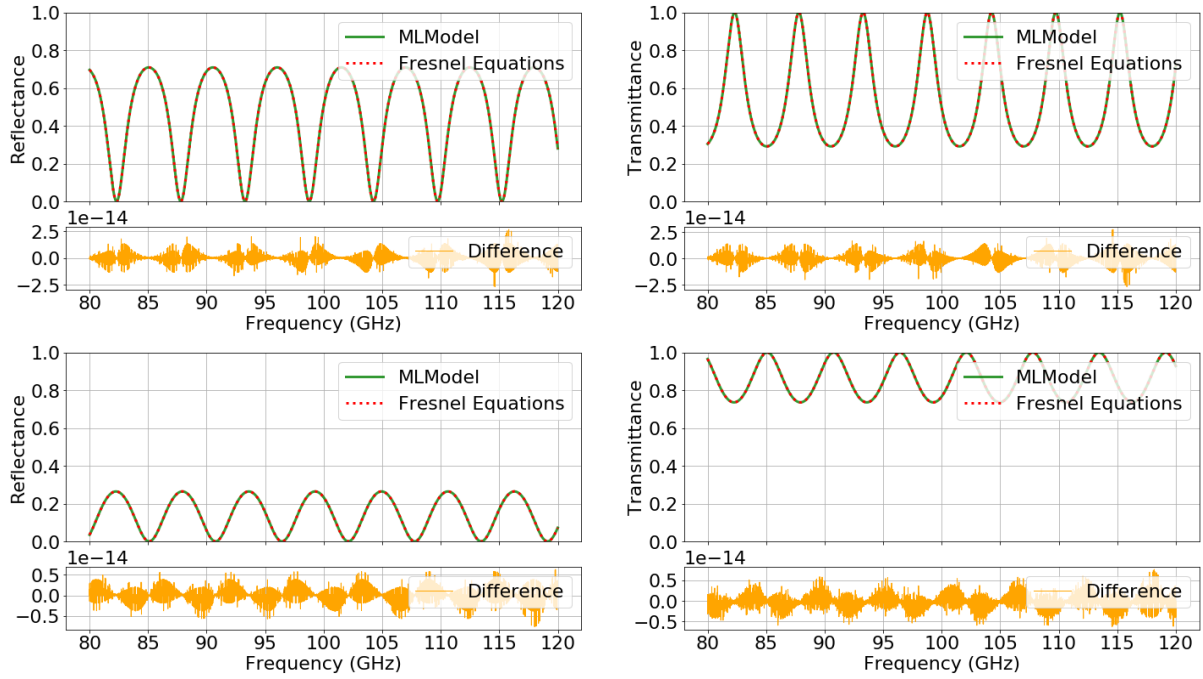


**Figure 5:** Comparison between Fresnel equations and the *MLModel* for p-polarized light. Top row is under a zero angle of incidence and the bottom row is under an angle of 60 degrees.

### 3.2.2 Other Models

The *MLModel* is compared with similar models used in [Feenstra, 2019] and [Kozlova, 2019]. In all comparisons the outcome of the models were exactly the same. All models were developed individually with very different code structure. With exactly the same outcome from three different models, and the test cases from textbooks and literature, we can assume that all models are correct.

### 3.2.3 Anti Reflection Coating

For our first simulation we test the *MLModel* on the theory of an anti-reflection coating. In optical systems, reflections of surfaces and lenses can cause unwanted effects. The reflections can cause stray light or standing waves in the setup. These unwanted effects can be reduced by using anti-reflection coatings. These coatings can be designed for surfaces to have zero reflectance in a specific frequency range. The most straightforward way of reducing the reflection on a surface is to apply an additional layer (coating) which has a dielectric constant intermediate of the that of the two mediums at the interface.

The anti-reflection coating has to be applied as seen in Figure 6. These anti-reflection layers are designed for a specific frequency, by having a layer thickness of a quarter wavelength. This results in destructive interference in the reflecting waves reducing the total reflectance. The dielectric constant of the layer is chosen such that the transmission from  $n_0 \rightarrow n_1$  and  $n_1 \rightarrow n_2$  is exactly the same (see Fig. 6). For a sample in free space, where  $n_0 = 1$ , the optimal dielectric constant of the anti-reflection coating is [Goldsmith, 1998]

$$\epsilon_{\text{coating}} = \sqrt{\epsilon_{\text{sample}}} . \quad (37)$$

The quarter wavelength thickness of the layer has to be tuned for a specific angle of incidence. For higher angles the path through the material is longer and should be accounted for. The optical thickness of the coating optimized for an angle of incidence  $\theta_i$  is

$$d_{\text{coating}} = \frac{\lambda_0 \cos \theta_i}{4\sqrt{\epsilon_{\text{coating}}}} . \quad (38)$$

To test the theory, an anti-reflection coating is applied onto a silicon slab with a thickness of 8 mm. The slab acts as a Fabry-Perot etalon, but will have zero reflectance for the frequency of interest. The input frequency range is  $1.2 \text{ THz} \pm 200 \text{ GHz}$  with the coating tuned on the central frequency of 1.2 THz. The dielectric constant for silicon is taken from [Feenstra, 2017] and is set as  $\epsilon_{\text{silicon}} = 11.66$ .

Using (37) and (38) the coating has properties  $\epsilon_{\text{coating}} = 3.41$  and  $d_{\text{coating}} = 33.8 \mu\text{m}$ . With the coating applied, the reflectance of the silicon slab is shown in Figure 7. The coating has to be applied on the interfaces on both sides of the slab and shows zero reflectance at the optimized frequency of 1.2 THz. If the layer is only applied on one side, only one of the two interfaces of the slab has reduced reflectance as can be seen in Figure 7.

This ideal coating would be a perfect application in systems to reduce the standing waves and scattered light. However, finding the perfect material with the right dielectric constant is difficult. In Table 5.1 in [Goldsmith, 1998] the dielectric constant is shown for multiple materials

at specific frequency ranges. From the table, the material closest to our ideal coating with enough information is Fused Silica. The dielectric constant is given as  $\epsilon = 3.82$ . The comparison between the ideal simulated case and the Fused Silica is shown in Figure 8. The Fused Silica shows a small non-zero reflectance at 1.2 THz, whereas the ideal perfect coating does have zero reflectance. The difference is small and there is only a reflectance of  $\sim 2\%$ . This small percentage of reflectance is not great, but also not terrible.

On top of the non-ideal material of the coating, the sample can also be under a small angle of incidence. This gives that the frequency for which the coating is tuned shifts, as the path through the coating becomes longer at higher angles of incidence. This shift can be seen in Figure 9 where the minimum of the reflectance shifts to higher frequencies. Overall the outcome of these simulations show that the theory can be applied on anti-reflection coatings, as the reflectance is zero where we expected it to be.

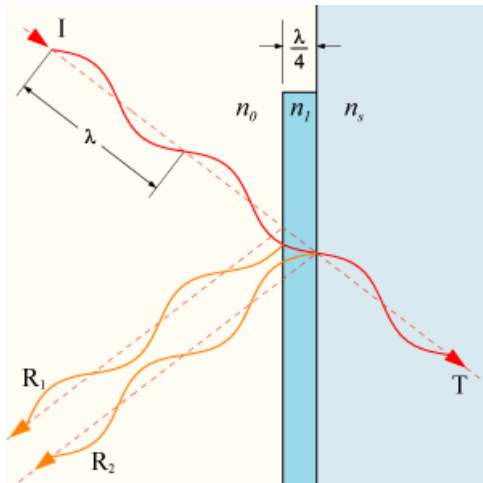


**Figure 6:** Schematic of an inverse impedance coating. Work by Bob Mellish.

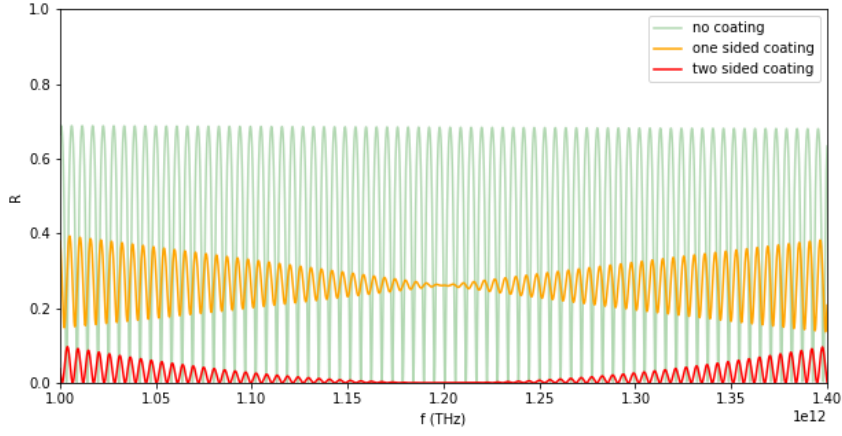


**Figure 7:** Simulation of perfect coating at 1.2 THz at zero angle of incidence. The reflectance is shown for when only a single coating is applied, and on both sides.

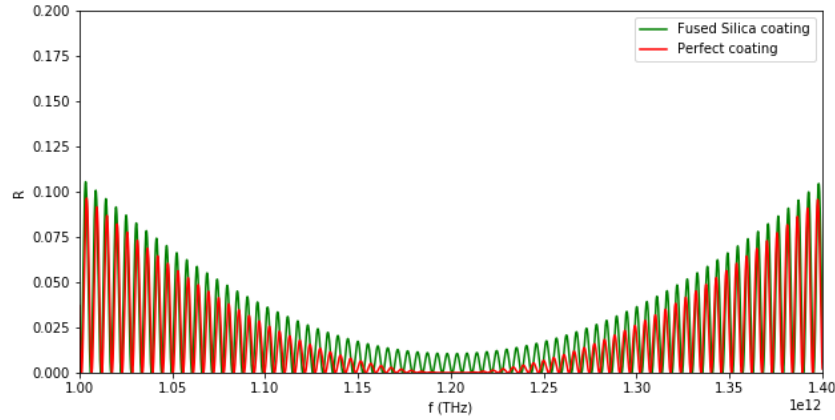


**Figure 8:** Perfect coating in comparison with the Fused Silica coating from Table 5.1 Goldsmith. The Fused Silica shows a small amount of reflectance.

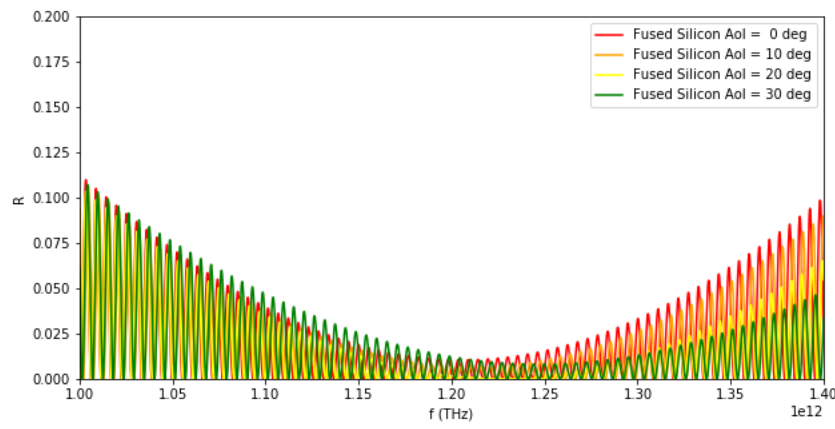


**Figure 9:** Multiple angles of Fused Silica coating. The optimized frequency shifts to higher values due to changes in the path length.

## 4 Reflective Half-Wave Plate

The objective of this internship was to automate a measurement setup and test a sample to test the multi-layer model. During the project we chose to make a reflective polarizing half-wave plate. The fabrication of the test sample was fully done at SRON Groningen with help of D. van Nguyen and H. Ode.

### 4.1 Purpose

The reflective polarizing half-wave plate, or *reflective resonant immersed half-wave plate*, is a design proposal by W. Jellema to use in SAFARI-VLW [Jellema, 2019]. It can be used to rotate the polarization state of the field of the sky without rotating the field itself, the slit or slit orientation of the SAFARI spectrometer. This is a necessary function of the instrument which still needs to be demonstrated. It is based around the theory described in Section 2, where a multi-layered system is setup which consists of two dielectric layers, a polarizing grid and a mirror. The configuration of the layers is shown in Figure 10. Incident radiation that comes in from the left first encounters a dielectric layer, then the grid and another dielectric layer. At last, there is a ground plane acting as a fully reflecting mirror, which causes the radiation to reflect out of the system via the first layers.

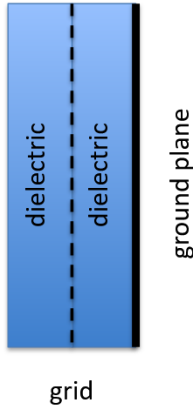


**Figure 10:** Reflective resonant immersed half-wave plate layout. *Provided by W. Jellema*

The reflective resonant immersed half-wave plate (*plate* from now on) is used to alter the polarization state of incident radiation. As only radiation perpendicular to the grid wires goes through the second dielectric layer, a phase shift occurs between the radiation with parallel and perpendicular states of polarization. The thickness of the dielectric layers can be optimized for a specific frequency. If the layers have a thickness of  $\lambda/4$  then a phase shift of  $\pi$  is introduced at this wavelength  $\lambda$ . The dielectric layers introduce optical resonances inside the system, which conserves the  $\pi$  phase shift over a slightly wider range than only the center wavelength  $\lambda$  creating a broader effective range of the device.

The plate can be used to alter the polarization state of incident radiation. If the plate, and thus the grid inside the plate, is rotated  $45^\circ$  with respect to the incident linear polarization state, then the polarization state of the reflected radiation will rotate by  $90^\circ$ . This is best seen in Figure 11, where the incident radiation is shown in red with its respective intensity components in the grid coordinate system  $(\hat{x}', \hat{y}')$ . Radiation parallel to the grid wires gets reflected, while radiation perpendicular to the grid wires travels longer through the second dielectric layer before being reflected by the back plate. This introduces a phase shift of  $\pi$  between the two vector components  $E_{x'}$  and  $E_{y'}$ , resulting in a rotated reflected polarization.

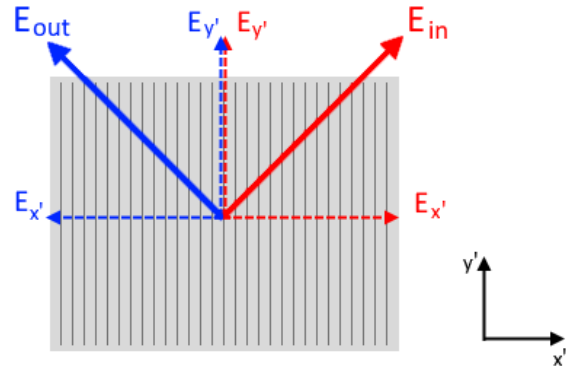


**Figure 11:** Polarization change due to reflective half-wave plate

The use case of the plate is shown in Figure 12. The plate is used in combination with a wire grid which polarizes the incident light on the device. Only radiation perpendicular to the grid wires reaches the plate. If the plate is rotated under an angle of 45 degrees, the polarization state of the light will rotate in accordance to Figure 11. The reflected radiation will now be parallel to the grid wires and reflect. This setup can be used in SAFARI-VLW and can solve for the field rotation problems induced by the current system. In this project we do not test the use case of Figure 12. We do test the response of the plate itself as shown in Figure 11.

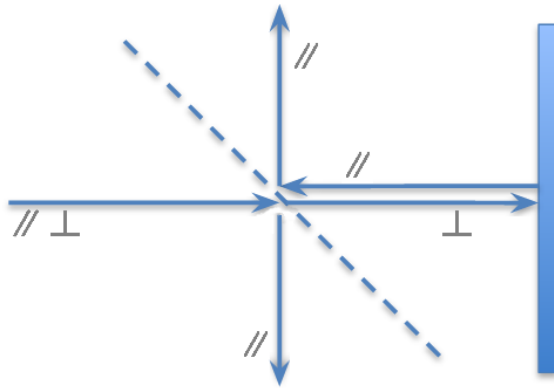


**Figure 12:** Use case of reflective half-wave plate. Incident radiation passes through a wire grid before reaching the reflective half-wave plate. The polarization states are shown with respect to the wire grid. *Provided by W. Jellema*

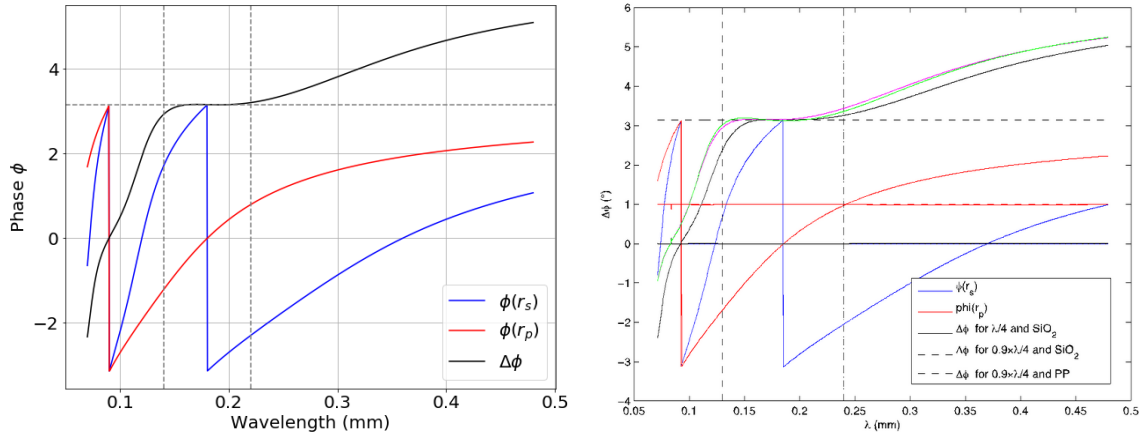
## 4.2 Modeling

In Section 3 we described a model for multi-layered systems. The *MLModel* can be combined with the Jones theory described in 2.3 to simulate the reflectance and transmittance of the plate. In this subsection we introduce and explain the simulations we eventually want to perform and measure on our self-made plate. We first simulate an ideal perfectly working plate (*model plate*) from theory and show the phase shifts between *s*-polarized light and *p*-polarized light in a broad wavelength range. Then a small demo is shown of the polarization state change induced by the model plate at different wavelengths.

### 4.2.1 Phase Shift

First we will model the phase shift induced by the model plate. The model plate will be tuned for the wavelength of 0.18 mm, so we expect to see a phase shift of  $\pi$  around this wavelength. The dielectric layers are tuned for a zero angle of incidence, which gives that the thickness of the dielectric layers is a quarter wavelength. The dielectric material is set to silicon dioxide ( $\text{SiO}_2$ ), which has a dielectric constant of 2.05. We also assume the grid and back plane are perfect reflectors, while the grid is also a perfect transmitter for the perpendicular polarization state. The grid is set to have a strip period of 2  $\mu\text{m}$  and strip width of 1  $\mu\text{m}$ . These layers are put into our model with the wavelength range 0.05 mm to 0.5 mm.

The outcome of the simulation is compared with a phase-shift plot provided by W. Jellema with the same parameters, to test the outcome of our model. The comparison between the two outcomes is shown in Figure 13. The data could not be plotted on top of each other, as only an image was available. The colors of the graphs are the same in both plots, to make it easy for the reader. We can see that the model produces similar results as the other model. This gives us a high confidence that our multi-layer model can be used to model a reflective half-wave plate.



(a) phase shift plot of model plate using our model (b) phase shift plot of model plate by W. Jellema

**Figure 13:** Comparison output phase shifts. The phase shift of the individual *s* and *p* polarization components are shown in blue and red respectively. The summed contribution, and therefore the full plate response, is shown in black.

Earlier it was touched upon that it is important to have dielectric layers in the device instead of air gaps. If there is an air gap between the grid and reflecting mirror instead of a dielectric layer, the plate is tuned for only a single wavelength. The presence of dielectric material, with a dielectric constant of around 2, broadens the wavelength regime in which the polarization is rotated by exactly  $\pi$ .

We again simulate the response of the model plate, but now the dielectric constant of the dielectric layers are set to 1, representing air gaps. The differences between the phase shifts of the dielectric layers and air gaps is shown in Figure 14. At the tuned wavelength of 0.18 mm we can clearly see that the plate with dielectric material has a broader range where the phase shift is  $\pi$ , whereas the plate with air gaps only has a phase shift of  $\pi$  at exactly 0.18 mm.

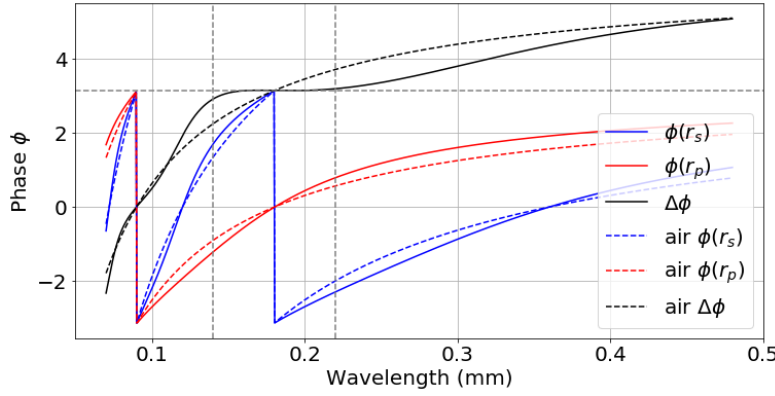


**Figure 14:** Dielectric layers vs. air layers

#### 4.2.2 Polarization State Rotation

The plate can be used to rotate the polarization state of linear polarized radiation as was shown in Figure 11. Incident radiation under an angle of  $45^\circ$  with respect to the grid inside the plate rotates to  $-45^\circ$  with respect to the grid lines in the tuned wavelength regime. We will reproduce this drawing by using our model to simulate linearly polarized incident radiation on a plate rotated  $45^\circ$  with respect to the radiation. We use the parameters of the plate as used in Figures 13 and 14 and compute the rotation of the radiation exactly at its tuned wavelength. In the global coordinate system  $(\hat{x}, \hat{y})$  we define the Jones vector for the incident radiation to be

$$\vec{E}_{\text{in}} = \begin{bmatrix} E_x \\ E_y \end{bmatrix} = \begin{bmatrix} 0 \\ 1 \end{bmatrix}, \quad (39)$$

which gets transformed to the grid coordinate system  $(\hat{x}', \hat{y}')$  via the rotation matrix  $\bar{R}$  (see Eq. (28)). The reflectance and transmittance coefficients are computed in the coordinate frame using a model of the plate and rotated back to the global coordinate system.

The Jones vector out of the plate is given by the model and is

$$\vec{E}_{\text{out}} = \begin{bmatrix} -1.00000000E + 00 \\ -5.43778911E - 11 \end{bmatrix} = \begin{bmatrix} -1 \\ 0 \end{bmatrix}, \quad (40)$$

which is the expected outcome within the numerical noise levels. The visual interpretation of the input vector, the model plate and the output vector are shown in Figure 15. We observe that the output of the model combined with Jones theory produces the same output as the theoretical expectation shown in Figure 11.

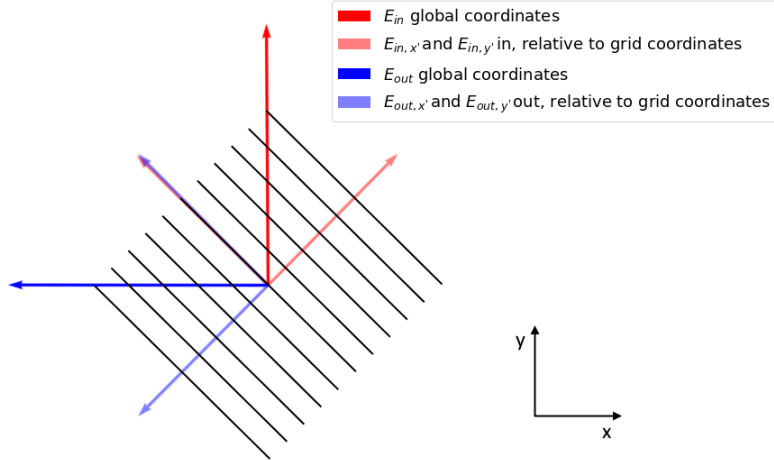


**Figure 15:** Output rotation results of reflective half-wave plate using Python

Above simulation only shows the outcome at exactly the tuned wavelength. But, we are also interested in the reflectance in a broader wavelength regime. We use the input vector (39) in the full wavelength range in the same setup as shown in Figure 15. The absolute response is shown in Figure 16, where we can see the reflected vertical and horizontal component of the Jones vector in the global coordinate space for the given wavelength range. We can see that the outcome is comparable to Figure 13, where the optimal rotation region between the dashed grey lines exactly overlap. This representation will actually be useful for the future experimental measurements, as the absolute values of the reflections in the horizontal and vertical polarization can be measured in our measurement setup and compared to simulations.

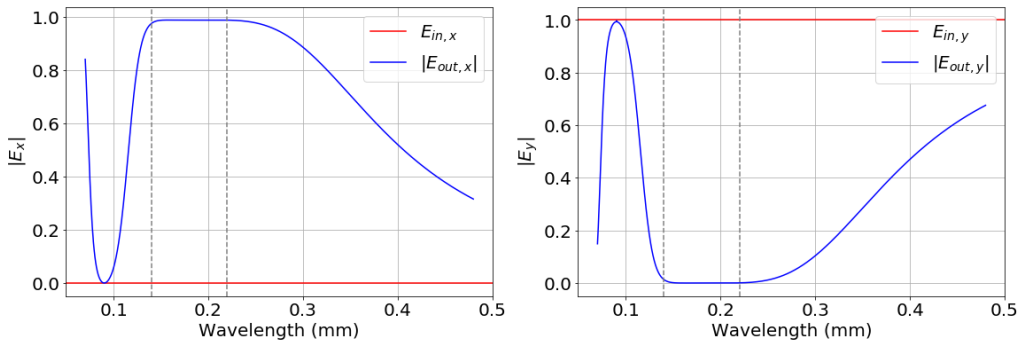


**Figure 16:** Model plate response at different wavelengths. The input Jones vector (red line) is defined as (39) as used in Figure 15 and is the same for all wavelengths. The output components are shown in blue.

## 4.3 Fabrication

Due to the limited time of the internship the fabrication of the test sample was done in a relatively short time with materials found at SRON. To build up the device we needed: dielectric material with the right dielectric constant, a way to make a polarizing wire grid, a reflective surface and glue to put all the layers together. After the assembly we simulate what the expected response is of the self-made plate and compare it to the theoretical ideal plate used above.

### 4.3.1 Dielectric Material

A handful of dielectric materials were tested for their transparency in the high frequency ranges that will be used. The materials were mostly circuit boards laminates: FR4, teflon and RT/duroid® 6002 laminate [Rogers Corporation, 2019]. Also kapton film was tested for its transparency. Of all the materials, RT/duroid® with a thickness of 0.79 mm showed the best results and was chosen to be used for the dielectric layers. We will from now on reference to this specific material as *Duroid*.

Two pieces are shown in Figure 17a and it shows that the Duroid laminate has copper on both sides of the plate, which is normally used for circuit etching. Copper is a very good conductor, so we used this layer to etch a strip wire grid as a polarizer (see Figure 17b).



**Figure 17:** Duroid samples

### 4.3.2 Polarizing Wire Grid

To etch the wire grid onto the Duroid sample, a grid template was made. This template is a drawing of the grid with desired dimensions printed on a transparent paper. A thin layer of photoresist was applied on the copper layer and illuminated with uv light while using the grid template. The plate was etched and the illuminated grid lines remained on the sample. The outcome of this process is shown in Figure 17b. The copper layer has a thickness of  $35 \mu\text{m}$  and the grid is etched with a strip period of 0.475 mm and strip width of 0.237 mm.

The grid was tested for its transmittance under different rotation angles. The first test was done by measuring the transmitted power at a fixed frequency for different angles and is shown in Figure 18. At the rotation angles of  $0^\circ$  and  $180^\circ$  there is no transmission measured, as the grid strips are parallel to the incident radiation and are fully reflective.

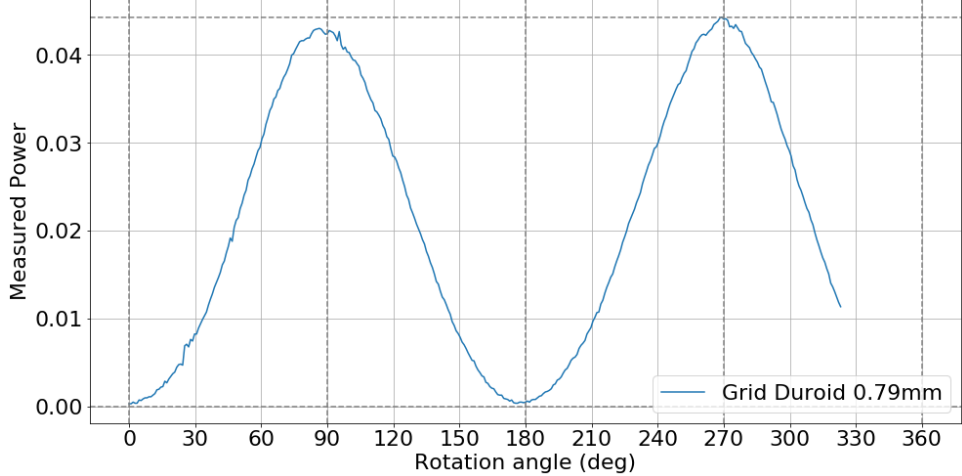


**Figure 18:** Transmission through grid for different rotation angles at fixed frequency input

Transmission scans were also done over the full frequency band at different rotation angles of the grid, which is shown in Figure 19. Also the mean is shown of the individual measurements via a dashed line. We can see that the measurements in Figure 19 coincide well with the expected transmitted powers at the given rotation angles. We again expect maximum transmitted power at the rotation angle of  $90^\circ$  and minimum power at the angles  $0^\circ$  and  $180^\circ$ . We also show the intermediate rotation angles of  $45^\circ$  and  $135^\circ$  where we expect the transmitted power to be at 50%. Besides the standing wave, that introduced itself after placing the grid sample in the setup, we can see that the power values are as expected.

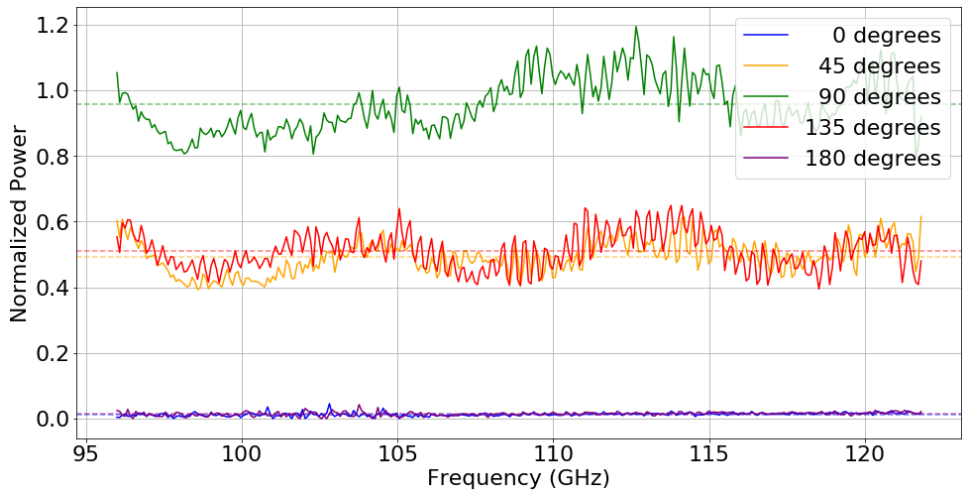


**Figure 19:** Transmission through grid over a frequency band for different rotations



(a) Plate parts

(b) Fully assembled plate

**Figure 20:** Parts of the reflective half-wave plate

#### 4.3.3 Ground Plate

For the ground plate, the reflective mirror of the full sample, an aluminum layer was used. The layer has a thickness of 2.00 mm and was a perfect mirror in our frequency range. The final parts are shown in Figure 20a before assembling and the full assembled plate is shown in Figure 20b. The parts are glued together and put into the oven for 30 minutes to form the complete plate. Information about the full plate is shown in Table 1. Additional tests were done to look at the contribution of glue between the dielectric layers. Comparison between before and after applying the glue showed no significant differences.

Layer	Material	Thickness	Information
1	Duroid	0.79 mm	
2	Copper Grid	35 $\mu$ m	$g = 0.477$ mm, $w = 0.237$ mm
3	Duroid	0.79 mm	
4	Aluminum	2.00 mm	Fully reflective mirror

**Table 1:** Layers of assembled plate.  $g$  and  $w$  denote the period and width of the grid strips.

#### 4.4 Simulations

With our self-made plate fully assembled we can now repeat the simulations which were done on the model plate shown in Section 4.2. At first we have to determine the tuned wavelength of our plate. We rewrite equation (38) to get a wavelength of

$$\lambda_0 = \frac{4d\sqrt{\epsilon}}{\cos \theta} = 4 \cdot 0.79 \text{ mm} \cdot \sqrt{2.94} = 5.42 \text{ mm} , \quad (41)$$

where  $\epsilon = 2.94$  as found in [Rogers Corporation, 2019] and the incident angle  $\theta$  set to zero.

The phase shift induced by our self-made plate is shown in Figure 21, which we will compare to the phase shift plot of the theoretical model plate as shown in Figure 13. At first we see that for our self-made plate that the region in which the phase shift is  $\pi$  is not as flat as the model plate. This is primarily due to the difference in dielectric constant of the dielectric layers. The plate works best for a dielectric constant  $\epsilon = 2$ , giving a perfect flat region. Duroid has a higher dielectric constant, resulting in this response around the tuned wavelength.

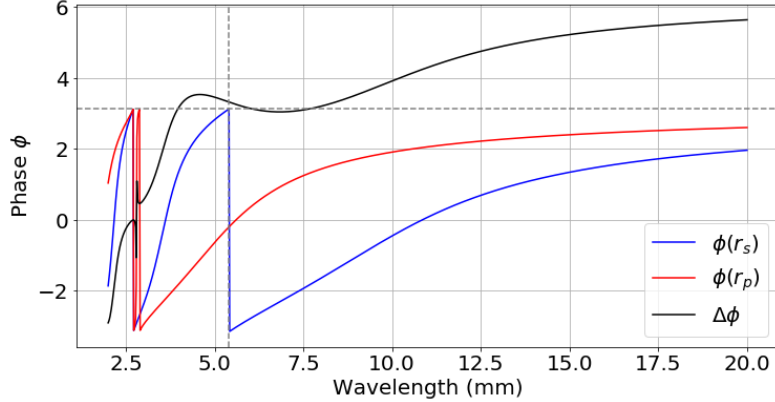


**Figure 21:** Phase shift plot of self-made plate at the resonance wavelength

We also simulate the ability of the self-made plate to rotate the Jones vector of the incident radiation. In Figure 22 we show the absolute values of the reflected horizontal and vertical components around the tuned wavelength of the plate. In comparison with the model plate, shown in Figure 16, there is a bit more chaos involved. At the tuned frequency, and its second resonance mode, we can see that the plate will be able to rotate polarization of the incident radiation. However, we again observe that the region in which this happens is not perfectly flat, due to the high dielectric constant. We also observe a sharp peak at around 3 mm, which is not observed in the smooth reflections shown in Figure 16. This is present due to the grid dimensions in our self-made plate, which we will discuss during the measurements in Section 6.

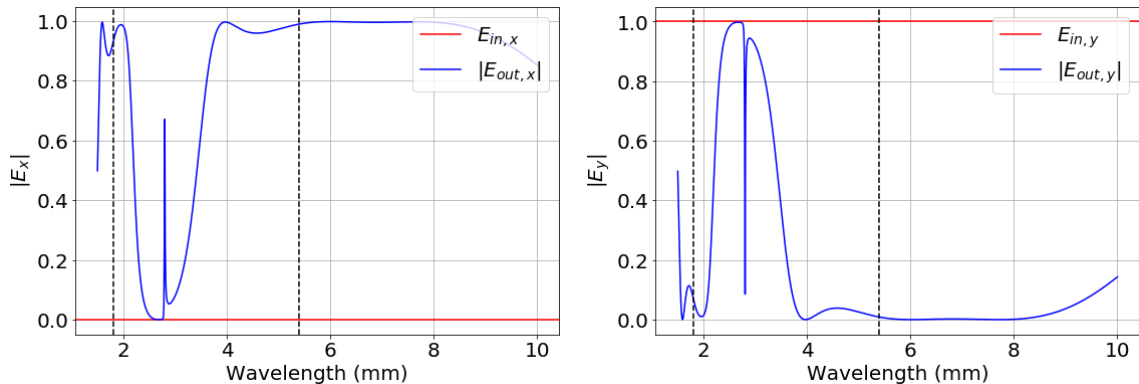


**Figure 22:** Self-made plate response at different wavelengths. The input Jones vector (red line) is defined as (39) as used in Figure 15 and is the same for all wavelengths. The output components are shown in blue. Quarter wavelength resonances are located at the dashed lines.

## 5 Experimental Set-up

Two experimental setups have to be build to test our model and to test the half-wave plate. To test the multi-layer model different dielectric materials are tested for their transmittance and fitted for their dielectric constant. The plate is tested for reflectance under different rotation angles. This gives that a transmission setup and reflection setup have to be put together. As only one detector was available, the transmission tests were done first and the setup was afterwards transformed into the reflection setup. Exact information about the orientation and distances of the equipment can be found in [Feenstra, 2019], as the same devices, source and lenses were used.

### 5.1 Devices

The setup consists of multiple devices to generate and to detect radiation. The devices used in the setups are shown in Table 2. Additional equipment is used to make sure the radiation beam propagates correctly through the system, two HDPE lenses with a focal length of 87.4 mm are used to make a collimated beam. Rotatable copper wire grids are used to get the light beam in the desired polarization state and to detect a specific polarization. At last we use attenuators to limit the power of the radiation beam such that the detector does not overload and to mitigate the effect of standing waves between the source and detector.

A synthesizer generates a tunable continuous waveform (CW) in the microwave range. This CW signal can be amplitude modulated to produce a pulsed input signal. The input signal is subsequently amplified and multiplied by a factor of 6 and coupled to free space by a horn. The emitted radiation is in the frequency range of 84 GHz to 124.2 GHz. The synthesizer is set to pulse with a frequency of 9 Hz. The pulse width is set to 55.55 ms, which gives a square wave shape.

The signal is detected using a Golay cell connected to a lock-in amplifier. A Golay detects absolute power, which on top of our signal includes background signals and noise. The lock-in amplifier is connected to the synthesizer and can filter the unwanted signal from the Golay. This gives that only the signal from the source is detected and the response of a device under test can be measured. The lock-in amplifier used in our setup can automatically obtain the pulse information from the synthesizer and calibrate the detected phase, which is very useful for automation of the setups.

Usage	Device
Synthesizer	Agilent 83640B
Detector	Unicam IR50 Infrared Detector (Golay cell)
Lock-In Amplifier	SR830 DPS Lock-In Amplifier
Power Supply	Agilent E3648A

**Table 2:** Devices used in setups

## 5.2 Automation

One of the objectives in this project was to make a fully automated setup to ease the amount of input during current and future measurements. We build up the setup using devices which could all be talked to via the GPIB interface. The synthesizer, lock-in amplifier and power supply are all controlled with Python using the PyVISA package. For each device a class was written for easy communication with the individual devices.

For the synthesizer we needed to be able to control the output state, output power, central frequency, frequency span and all settings for the pulse modulation of the output signal. With these actions we could start a measurement with a single script, which can safely turn on, change frequency and turn off the output signal.

The lock-in amplifier model we use already had buttons (and functions) to automatically detect the frequency and offset of the pulse generated by the synthesizer. A class was made to control the reference input and to be able to calibrate the device. The detector output could also be retrieved by reading out the display values.

The last device is the power supply, which was used for a rotatable holder for a device under test. The power supply voltage and output state could be controlled to safely use the device. The rotatable holder was controlled via a serial port by using the NI-DAQmx wrapper python package and a stepper motor controller.

The automatic setup is also meant for future measurements of the SRON Fabry-Perot etalon. All classes and the main program are provided along our *MLModel* on GitHub<sup>3</sup>. A measurements consists of simply executing the main script. Parameters can be set in the script for frequency range, output power and rotation settings and more. Data is automatically stored in text files with corresponding documentation. The data files can be read out by the users favorite visualization tool.

## 5.3 Transmission Setup

The first setup built up during this internship was for transmittance tests. This setup is used to test different materials for their transmittance and to test the model described in Section 3. The same setup is used in [Feenstra, 2019] and is shown in Figure 23, where the transmittance of a Fabry-Perot system is measured. One difference is that no polarizing grids are used in our transmission setup, as the light source already outputs *s*-polarized light. The lenses are aligned such that there is a collimated beam with an effective diameter of 45 mm at the test sample.



**Figure 23:** Transmission setup used in [Feenstra, 2019]

<sup>3</sup><https://www.github.com/Formsma/MLModel>

The test source showed to be too powerful for the detector. To not damage the detector two attenuators, -9 dB and -10 dB, are placed in the setup at the grid locations of Figure 23. In turn, this also helped to significantly damp the unwanted standing waves in the setup. Each round trip between the source and detector passes twice through both attenuators attenuating the standing wave by a total of 38 dB. Reference measurements are done by measuring over the full frequency band with no sample between the lenses.

During experiments with this setup the transmittance of different dielectric materials is measured. Also a short test was done with the Fabry-Perot used in [Feenstra, 2019] to see if results are similar. Data analysis of the experiments is done in Section 6.

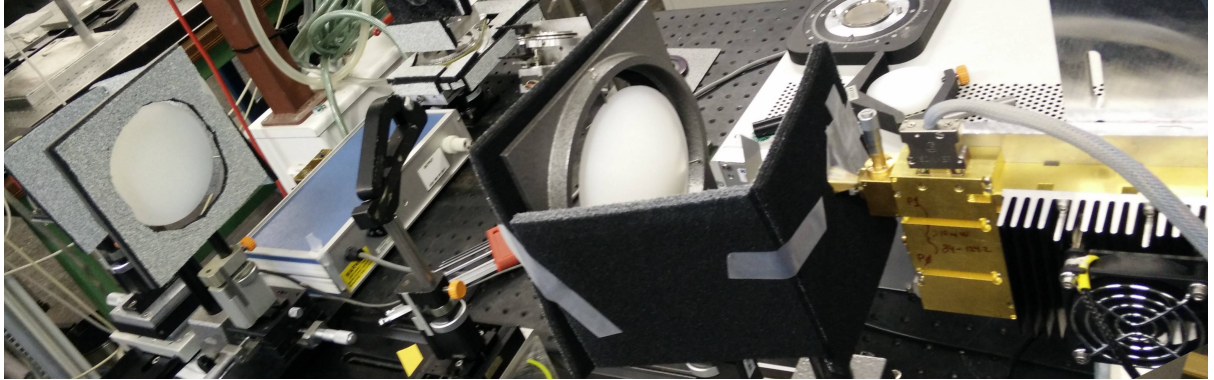


**Figure 24:** Transmission setup

#### 5.4 Reflection Setup

After all the transmission tests of materials and testing our model, the reflectance setup was build. This setup was solely for testing the reflective half-wave plate build in Section 5. The setup is shown in Figure 25 and 26, where both a drawing and a picture are shown. As we had a lot of interest in the polarization state of the incident and reflected light of the plate (DUT in Fig. 25), two wire grids were added to the setup. Light from the source passes through the first grid to ensure its polarization state. The grid lines of the grid next to the source are in a horizontal position, which gives that only *s*-polarized light passes through. Afterwards, the light passes through a 0.350 mm Silicon beamsplitter before reaching the device under test. The reflected light goes to the detector through the last grid. This grid is used to determine the measured polarization state, either vertical *s* or horizontal *p*-polarized.

A test sample can be mounted in a rotatable mount which is controlled by a stepper motor. Reference measurements can be done by putting a fully reflective mirror inside the mount and do a frequency scan for different rotations.

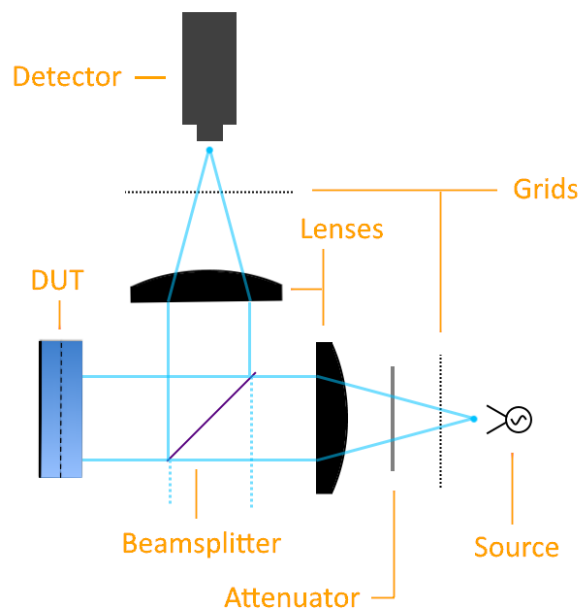


**Figure 25:** Reflection setup schematic

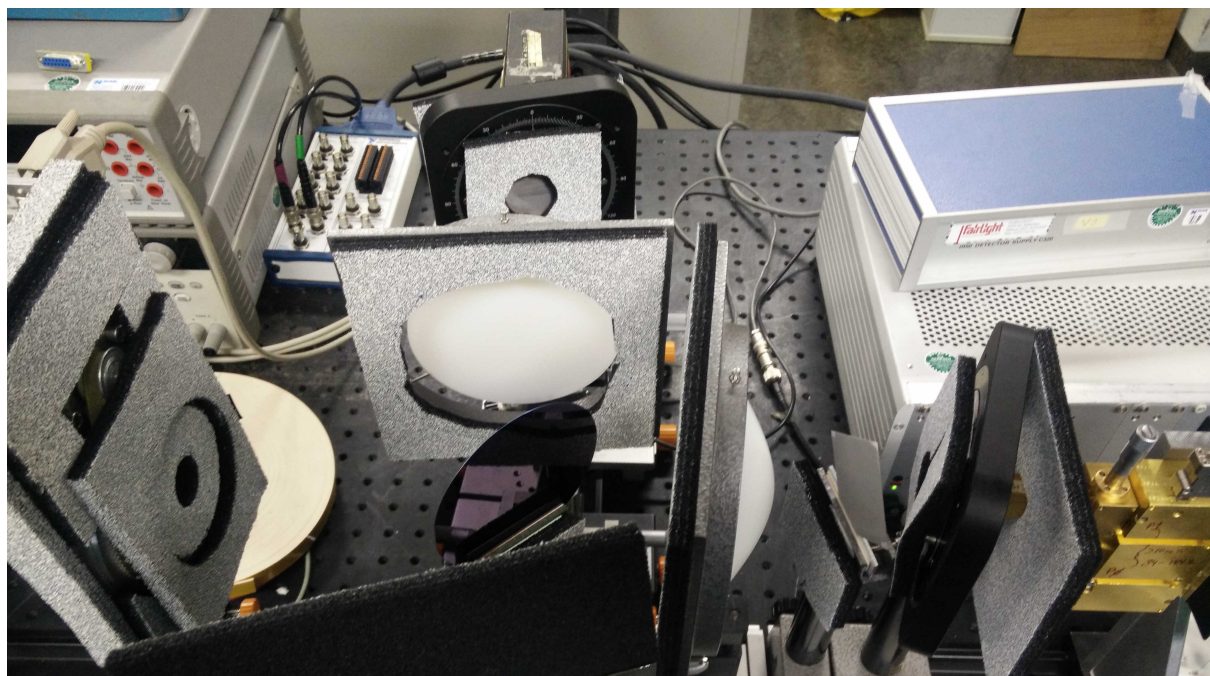


**Figure 26:** Reflection setup

## 6 Data Analysis

Experiments were done with different dielectric materials and their transmittance was measured. Also, for our self-made reflective half-wave plate the reflectance was measured under different angles of rotation. The data was inspected and also tests of our model were made to ensure that it works.

### 6.1 Transmission Tests

The materials that are measured for their transmittance are shown in Table 3. However, as Kapton and Teflon did not show good results in the initial measurements, there are no full frequency scans and data inspection of these materials. Also, FR4 was only used to test the method to make a grid on the layers.

Material	Thickness
HDPE	6.93 mm
HDPE	9.22 mm
Duroid	0.79 mm
FR4	1.54 mm
Teflon	0.52 mm
Kapton	0.11 mm

**Table 3:** Available dielectric materials

#### 6.1.1 HDPE

The first measurements were done with slabs of HDPE of two different thicknesses. These tests were primarily done to ensure that the model works with well known materials. As these slabs are single layer systems, we can also fit for the transmittance with the Fresnel equations. The data, normalized data and fits are shown in Figure 27 and 28 for the thicknesses 6.93 mm and 9.22 mm respectively.

The results of the model fits are shown in Table 4, where the values are compared with theoretical values. The theoretical values are derived from multiple measurement values found in [Goldsmith, 1998] in our frequency regime. The outcome of the measurements are very similar to the theoretical values.

Material	Theory $\epsilon$	Fit $\epsilon$	Theory $\tan \delta (10^{-4})$	Fit $\tan \delta (10^{-4})$
HDPE 6.93 mm	$2.31 \pm 0.08$	$2.305 \pm 0.004$	$5 \pm 3$	$5 \pm 1$
HDPE 9.22 mm	$2.31 \pm 0.08$	$2.365 \pm 0.003$	$5 \pm 3$	$8 \pm 2$

**Table 4:** Results HDPE. Theoretical values can be found in Table 5.1 of [Goldsmith, 1998]

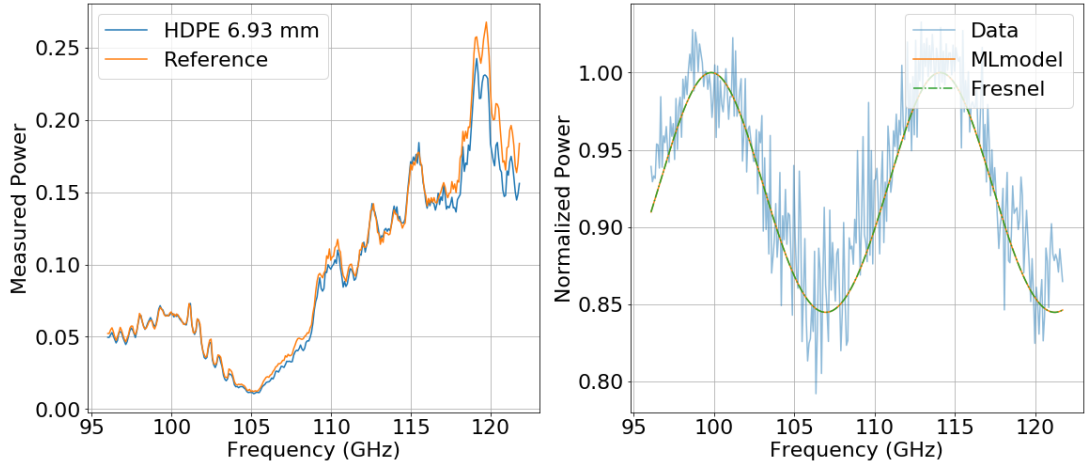


**Figure 27:** Transmission measurement of HDPE 6.93 mm

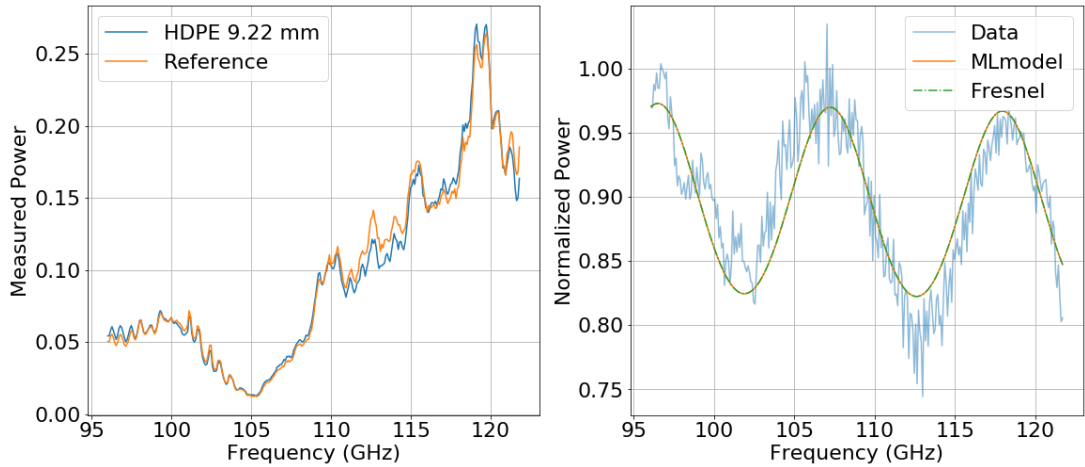


**Figure 28:** Transmission measurement of HDPE 9.22 mm

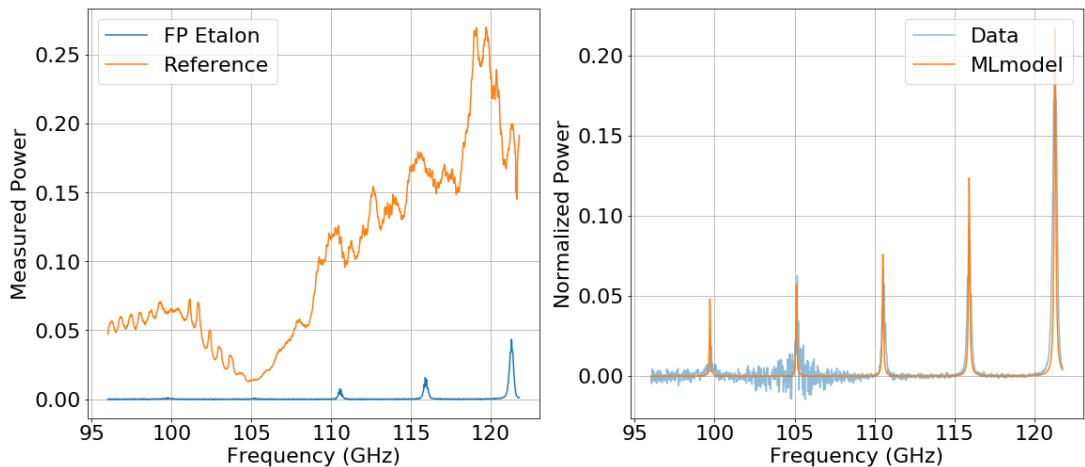


**Figure 29:** Transmission measurement of Fabry-Perot etalon

### 6.1.2 Fabry-Perot etalon

The original goal of this internship project was to repeat the measurements of [Feenstra, 2019] in a different frequency range. As we could not do this due to unforeseen circumstances, we did measure the transmission of the Fabry-Perot once in the same frequency range for a model test. One transmission measurement is done and the full scan is shown in Figure 29. The results of the model fit are shown in Table 5. Because at low frequency there is a lot of noise, three different fits are done on the data. The fits can be seen in Appendix C and their respective frequency range is also shown in Table 5.

We observe an offset with the values found in [Feenstra, 2019]. This offset is probably due to the different scale of measurements done on the Fabry-Perot etalon. Our single measurement can not be compared with the vast amount of scans at different angle of incidence done in [Feenstra, 2019]. The fit values do get closer to theoretical if we only fit data at higher frequencies, as the signal to noise is higher at these points.

Material	Theory $\epsilon$	Fit $\epsilon$	Theory $\tan \delta (10^{-4})$	Fit $\tan \delta (10^{-4})$
Full	$11.659 \pm 0.002$	$11.50 \pm 0.06$	$6 \pm 1$	$16 \pm 8$
110 - 124 GHz	$11.659 \pm 0.002$	$11.52 \pm 0.06$	$6 \pm 1$	$16 \pm 4$
115 - 124 GHz	$11.659 \pm 0.002$	$11.55 \pm 0.04$	$6 \pm 1$	$17 \pm 9$

**Table 5:** Results SRON Fabry-Perot. Theoretical values can be found in [Feenstra, 2019]

### 6.1.3 RT/duroid

Above results of the HDPE slabs and the Fabry-Perot etalon give us great confidence in the model. We will now apply the model to more experimental measurements of the thinner Duroid sample. Multiple measurements are shown in Figure 30 of a single 0.79 mm Duroid slab. For each measurement a fit is made and the values corresponding to an average of the fits are shown in Table 6. In the plot, a broader frequency regime is shown with a transmittance curve for the theoretical values of Duroid. This gives a clear indication that a fit for this transmittance peak has to be found.

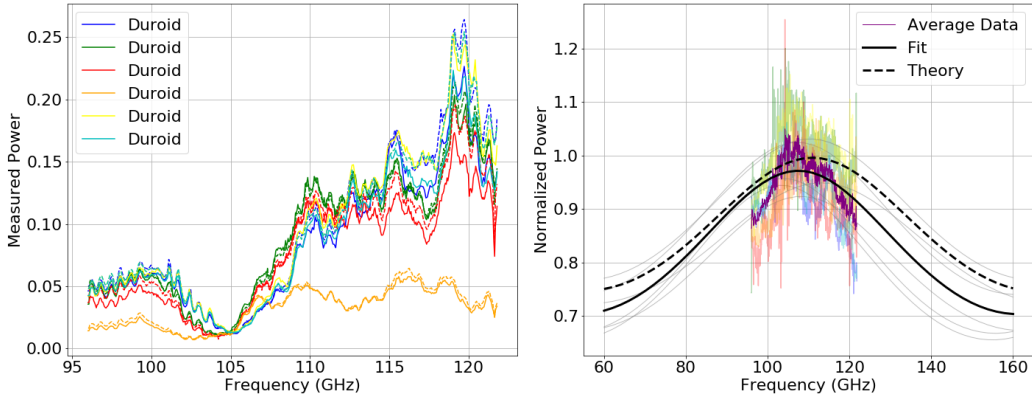


**Figure 30:** Multiple transmission measurements of Duroid 0.79 mm. The solid black line indicates the average of all data fits, while the dashed line shows a model using the theoretical physical parameters of Duroid.

Material	Theory $\epsilon$	Fit $\epsilon$	Theory $\tan \delta (10^{-4})$	Fit $\tan \delta (10^{-4})$
Single Duroid slab	$2.94 \pm 0.04$	$3.1 \pm 0.2$	12	$104 \pm 71$
Duroid Fabry-Perot	$2.94 \pm 0.04$	$2.59 \pm 0.01$	12	$43 \pm 13$

**Table 6:** Results Duroid. Theoretical values can be found in the data sheet [Rogers Corporation, 2019] and are for  $f = 10$  GHz

The fitted value for the dielectric constant shows good overlap with the theoretical value found in the data sheet of the manufacturer. However, the value for the loss tangent is an order bigger than the theoretical value with high uncertainty. This big difference is due to the poor normalization of the data. As can be seen in Figure 30, the fit has a high accuracy on finding the transmission peak, but with a low precision. The dielectric constant is only dependent on the shift of the peak in frequency, whereas the loss tangent is difficult to fit due to the dependency on the height and sharpness of the peak. The single Duroid slab is too thin to make a good model fit in our available frequency range. Accurate measurements of the dielectric properties of thin films generally requires a very large bandwidth or local resonant features, which we unfortunately both lack.

In order to try to get a better fit for the loss tangent of Duroid, we construct a very simple Fabry-Perot device of two Duroid slabs. This is done by putting double-sided tape pieces with a thickness of 1 mm in between two samples. This forms a Duroid-air-Duroid Fabry-Perot system in which we have more internal reflections and absorption. The fit is shown in Figure 31 and the corresponding fit values can be found in Table 6. Unfortunately the theoretical data plot shows that there are no interesting features in our frequency range and the fit is also not very accurate.

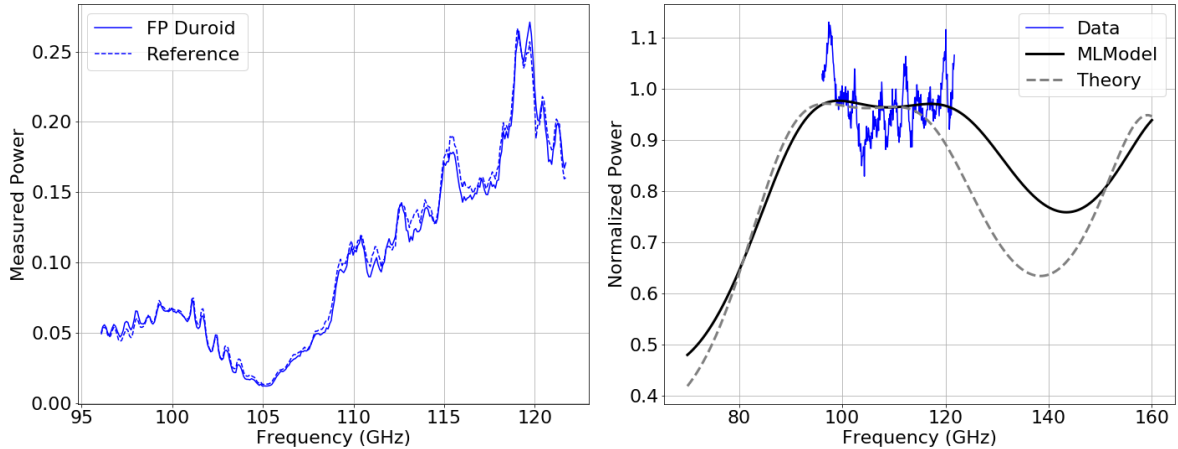


**Figure 31:** Transmission measurements of Duroid Fabry-Perot. The solid black line indicates the fit on the data while the dashed line shows a model using the theoretical physical parameters of Duroid.

## 6.2 Reflection Tests

The reflection tests are carried out on the self-made reflective half-wave plate. At all times there is vertical *s*-polarized light incident on the device as described in Section 5.4. The *s*-polarized light is defined as vertical polarized light in the lab coordinate system and *p*-polarized as horizontal polarized light, as was used in the simulations in Section 4.2 and shown in Figure 15. Two different measurements are done, where either the reflected *s*-polarized light is measured or the reflected *p*-polarized light. As the device should be able to rotate the polarization state of incident light, we expect an inverse correlation between the measurements. That is, where there is low *s*-polarized reflected power, there should be high reflected *p*-polarized power.

The expected outcome of the measurements is shown in Figure 32, where the device is put under a rotation angle of  $45^\circ$ . At this angle the incident *s*-polarized light will be fully rotated into *p*-polarized light around the resonance frequencies. In Figure 32 we show the frequency range of our setup overlaid on the data of Figure 16. Unfortunately, we can see that in the frequency range of the setup the plate is not great at rotating the incident light. However, we still observe that there is a pointy feature at 107 GHz where the polarization state is rotated, which can be measured. The presence of this feature at 107 GHz can be traced back to the dimensions of the grid inside our self-made plate. The grid strip width and period seem to be too big for our frequency range, probably resulting in extra resonances inside the system. We will for now accept the presence of this resonance feature and later discuss in Section 7 what it is.

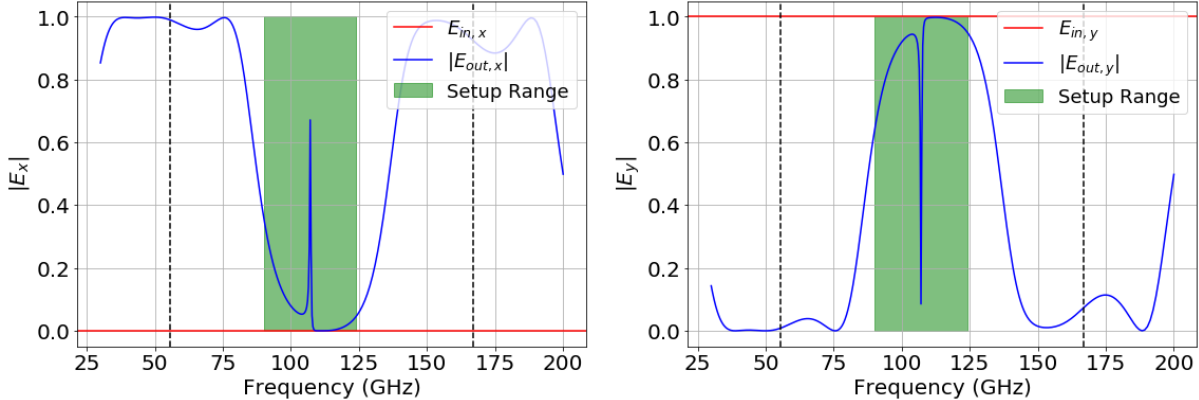


**Figure 32:** Simulation of reflected light on our plate at a rotation angle of  $45^\circ$  with only *s*-polarized incident radiation. The frequency range of our setup is highlighted with green.

### 6.2.1 *s*-polarization

The first experiment is done in which the detector only measures vertical *s*-polarized reflections. A reference measurement is done by placing a perfect mirror at the location of the device. We measured the reflections of the device by doing full frequency scans over our bandwidth while rotating the device in between scans. All the measurements at different rotation angles are shown in Figure 33. We can see that for multiple rotation angles the resonance feature is again visible at 107 GHz just as in the simulation in Figure 32. The most notable differences between all the measurements is the depth of the feature.

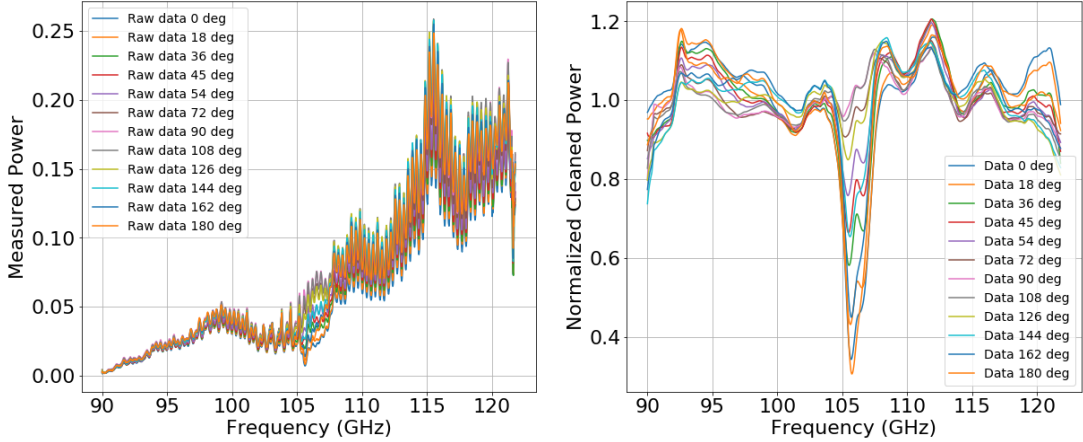


**Figure 33:** Measurements of *s*-polarized light from the plate at different rotation angles

Parameter fits on all individual measurements are shown in Appendix D. We highlight two of the fits in Figure 34. A theoretical curve is also shown in the figures using theoretical values for Duroid shown in Table 6. We can see that there seems to be a slight offset in the resonant feature location, as it is more located near 105 GHz. This shift can be traced back to a difference in dielectric constant between the data and theoretical values. Averaging all the models gives that the dielectric constant of Duroid in our frequency range is  $\epsilon = 3.04 \pm 0.03$ .

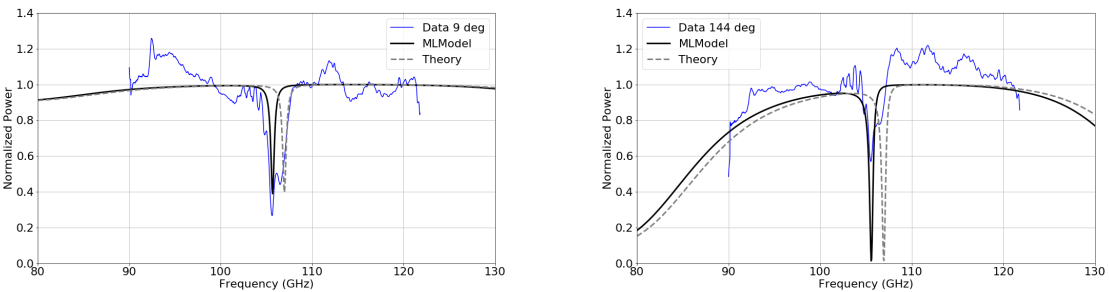


**Figure 34:** Fits on reflective half-wave plate

The trend we see in the data is that at 0 degrees of rotation the feature at 105 GHz is the deepest, while the theoretical curves have the deepest feature at a rotational angle of 45 degrees. Using different parameters for the grid of the plate shows that the feature depth is dependent on the grid period and width. This gives a discrepancy between our grid and a theoretical grid, giving us to believe our grid does not work as well as expected.

### 6.2.2 $p$ -polarization

At last the reflectance of  $p$ -polarized light is measured and therefore the ability of the plate to rotate the polarization state of the incident radiation. As we saw that the  $s$ -polarization measurements showed overlap with the models, we expect to see a peak at 105 GHz. A frequency scan is done on the plate at a rotational angle of 45 degrees. Measurements on other rotational angles showed no measured power above the noise levels and can therefore not be used for fitting.

The model fit on this data shown in Figure 35. Apart from the differences at the ends of the data, we can fit for the feature at 105 GHz. This results in a dielectric constant for the Duroid layers of  $3.03 \pm 0.08$ . Of all possible rotational angles of the plate, there is only a tiny amount of power detected when the half-wave plate is at its optimal rotation at  $45^\circ$ .

The peaked feature at 105 GHz shows that the plate is able to rotate the polarization state of some incident radiation. As expected in our frequency range, the plate shows overall poor performance in rotating most of the incident  $s$ -polarized light. Simulations are also performed to look at the influence of equipment in the setup, such as polarization grids and the beamsplitter. The beamsplitter has to reflect  $p$ -polarized light while under an angle of  $45^\circ$ , which decreases the power of the signal through the setup. This explains the low measured power of the  $p$ -polarized light in the most optimal rotation and the lack of measurable signal in the other rotations of the plate.

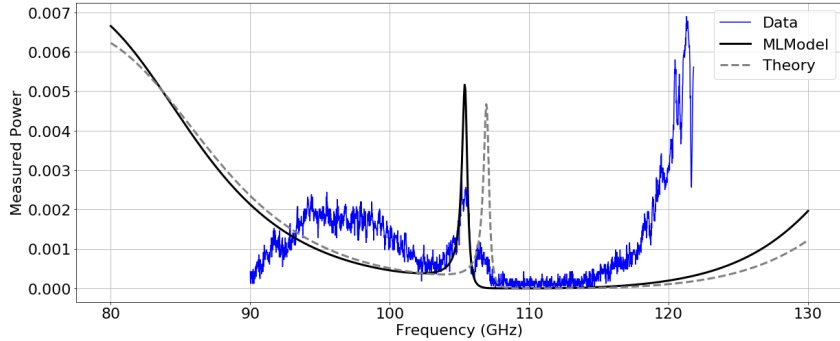


**Figure 35:** Measurement of  $p$ -polarized light from the plate at  $45^\circ$  rotation angle

## 7 Discussion

During and after the project a few things came up to discuss for future iterations of this project. This includes results from measurements, but also observations done on building the model and the reflective half-wave plate.

### Model

The *MLModel* was developed with the objective to model the response of the Fabry-Perot etalon from [Feenstra, 2019]. This was done successfully and showed good overlap with measurement results. The model can also consider the change in layer thickness due to temperature changes. It can include the *coefficient of thermal expansion* of materials to model the changes in thickness of the layers due to temperature differences. However, this is never tested, as the CTE component was never used in this project. Documentation and code comments are available in the model code if this needs to be implemented.

### Fabry-Perot measurements

To test the model we did a single measurement of the Fabry-Perot device. This gave slightly different results as reported in [Feenstra, 2019]. This difference can be accounted for by the different amount of measurements done on the device. In [Feenstra, 2019], multiple measurements are done at multiple angles of incidence, giving a more accurate and precise result than our single measurement. There was no time available for extensive measurements, as the self-made plate had to be tested.

### Duroid measurements

The first measurements of a single slab of Duroid (Fig. 30) showed a sharp transmittance peak in the center of our frequency regime. The location of this peak is primarily dependent on the dielectric constant of the Duroid layer. The shape and height of this peak are influenced by the loss tangent and angle of incidence of the radiation on the sample. Due to the good accuracy of the peak location, we get a good fit for the dielectric constant. However, the shape of the fit is not a good match for the data. This can be accounted for by insufficient normalization done on the data. The Duroid slab is also too thin to see a full interference cycle in our frequency regime. If multiple measurements at multiple angles of incidences were performed, we could get a better understanding of this dependence and probably a better fit for all parameters.

### Plate Fabrication

A reflective resonant immersed half-wave plate was made to test for the use case described in Section 4.1. The plate was build with materials found at SRON, so only a few options for dielectric materials were available. The choice of dielectric material was a Duroid laminate with a thin layer of copper on both sides. The grid inside the device was etched out of the pre-applied layer of copper. Due to limitations to etching, the grid period was chosen to be approximately 0.5 mm. Compared with the frequency range of the setup, the grid period is only 5 times smaller than the biggest wavelength.

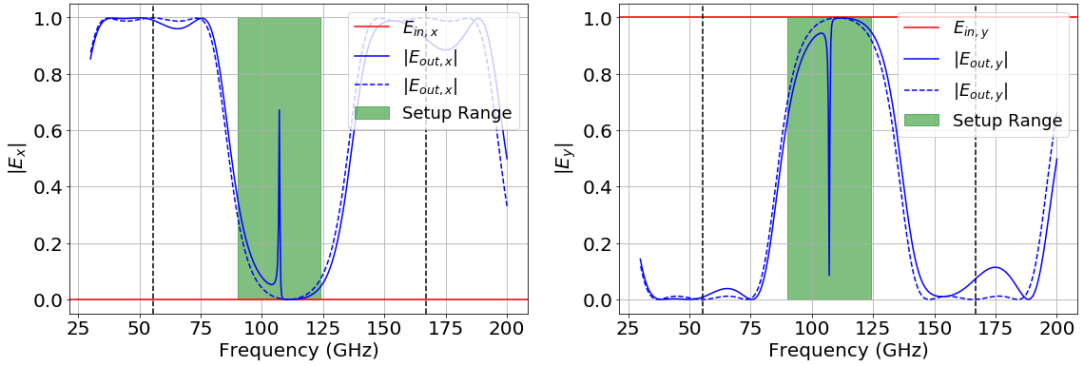


**Figure 36:** Reflected light if  $s$ -polarized light is incident on a  $45^\circ$  rotated plate. The dashed line represents a plate with a wire grid defined by a strip period and width much smaller than the wavelength of incident radiation.

### Plate Measurements

The measurements show that the self-made plate does not function in the available frequency range of our setup. This result was expected, as the plate was not tuned for this frequency range. The simulations and measurements did show an interesting peaked feature at 105 GHz. This anomalous effect could be traced back to the polarizing wire grid in our plate, as tuning the grid strip width to lower values removed the feature (see Figure 36). We believe that the feature arises due to some resonances inside the system, as the grid clearly shows non-optimal behaviour. In the optimal case the grid period has to be at least 16 times smaller than the wavelength of the incident radiation. For future designs it needs to be fully understood to ensure it will not show up again. The easiest method to avoid this resonant feature is by making a polarizing grid with dimensions much lower than the wavelength of the incident radiation.

A positive side of the unexpected resonant feature is that its location is fully dependent on the dielectric constant of the layers in the system. We could fit for the resonant peak and find a very accurate value for the dielectric constant of Duroid. If we had made a better polarizing grid inside our system, with lower values for the grid dimensions, the resonant feature would not be present. This would increase the difficulty to fit for our data significantly, as can be seen in Figure 36. This is a nice illustration of how the dielectric properties of a thin layer can be measured by embedding it in a resonant structure and fitting a model to the observed response.

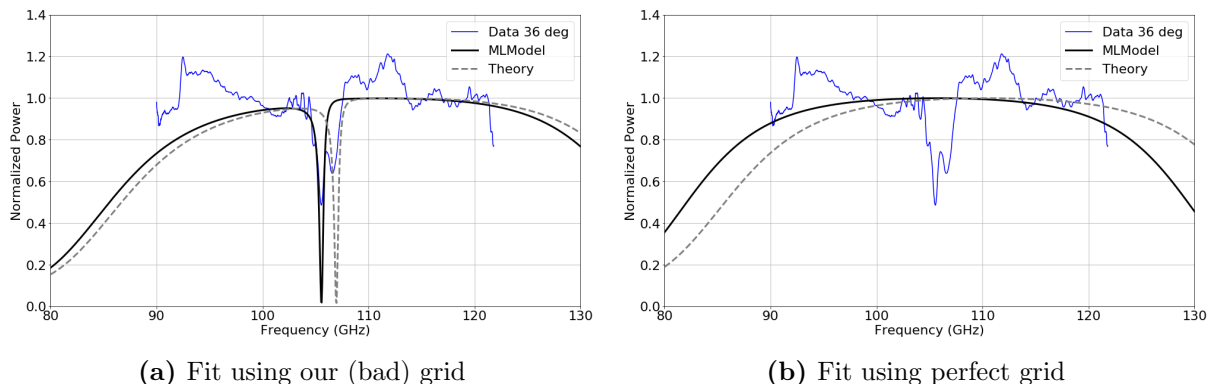


**Figure 37:** Comparison between a grid approaching the wavelength limit and a perfect grid

### **FIT Stage**

This internship was part of the course *stage fysische informatietechniek* at the University of Groningen. This course is based around making students familiar with the aspects of information technology and the control of physical processes. This internship did succeed in these points, but it did cost a lot of time to set up and work out. As the original goal of the internship shifted due to global delivery problems of helium, more time needed to be invested in this project. Only a bit of extra time was available, resulting in an absence of extensive measurements at different angle of incidences. For a future project, with more time, the reflective half-wave plate is a very interesting concept to test and to implement in a real instrument someday.

## 8 Summary and Conclusions

The reflectance of a *reflective resonant immersed half-wave plate* was measured for its ability to rotate the linear polarization state of incident radiation. This is a system composed of a polarizing wire-grid surrounded by a dielectric layer on each side and a reflective mirror on one side. Incident radiation on this system undergoes internal reflections and can be compared to a complicated Fabry-Perot etalon.

The transmission line theory is used to describe the response of the plate. This theory can be applied to get the reflective and transmissible properties of the dielectric layers in a system. A generic model was build using this theory, which can simulate the reflectance, transmittance and absorption of any multi-layered dielectric system. This model was tested using different dielectric materials and with literature examples. Our model showed good results and was compared with other models, showing perfect overlap.

The reflective half-wave plate used in this project is a self-made device build at SRON Groningen. The device consists of RT/Duroid 6002 plates for the dielectric layers, a copper grid etched on the layers as a polarizer grid and an aluminum back-plate as a fully reflective mirror. The components are glued together to make up the full assembled device.

In order to test the device, a fully automated experimental setup was built. The setup can be controlled using Python scripts and all devices are controlled individually via custom-made classes. An extensive measurement can be performed by entering only a few parameters about the experiment. The setup will be used for future projects to measure the transmittance and reflectance of other systems.

Experiments were done with the device to measure the reflectance at different frequencies. The detector in the setup could either detect *s*-polarized light or *p*-polarized light and the ability to change the polarization state could be derived. We noticed quickly, via simulations and measurements, that the self-made plate was not tuned for the available frequency range of our setup. Therefore, only the out-of-band response of the plate was measured showing very little *p*-polarized light. As this was reasonably well in line with the predicted response, we also observed an unwanted feature in the data due to non-ideal grid behaviour. In this resonant feature we could observe a little amount of *p*-polarized light, but this was not representative for the intended use case of the plate. The work in this project gave much insight in the process of making and measuring a simple reflective resonant immersed half-wave plate and its results and the model will be useful for further research.

The self-made device gave us the ability to measure the dielectric constant of RT/Duroid 6002 very accurately, due to the resonant feature found in the data. The dielectric constant in the frequency range 84 GHz and 124 GHz was found to be  $3.04 \pm 0.03$ . This is close to the literature value of  $2.95 \pm 0.04$  measured at 10 GHz.

## References

- [Feenstra, 2017] Feenstra, C. (2017). *Feasibility study of an experimental method to determine the loss tangent of silicon at millimeter wavelength for cryogenic temperatures*. University of Groningen, BSc Thesis.
- [Feenstra, 2019] Feenstra, C. (2019). *Feasibility study on the resolution of a FP etalon at millimeter wavelength and cryogenic temperatures*. SRON Groningen, Internship Report.
- [Goldsmith, 1998] Goldsmith, P. F. (1998). *Quasi-optical Systems*. IEEE Press, Chapman and Hall, Publishers, New York.
- [Hecht, 2002] Hecht, E. (2002). *Optics 4th*. Addison-Wesley: Reading, Mass.
- [Jellema, 2019] Jellema, W. (2019). *Reflective resonant immersed half-wave plate for SAFARI-VLW*. Presentation May 27th, 2019, unknown location.
- [Kozlova, 2019] Kozlova, D. (2019). *Design and Fabrication of a Narrow Bandpass Interference Filter*. University of Groningen, BSc Thesis.
- [Rogers Corporation, 2019] Rogers Corporation (2019). *RT/duroid®6002 High Frequency Laminates*.

## Appendix

### A: Derivation of Fresnel Equations

A short description and derivation of the Fresnel Equations into the reflectance and transmittance equations of a Fabry-Perot etalon. This is a short summary page of [Feenstra, 2017] section 2.3 and 2.4.

The reflection and transmission coefficients of light depends on its polarization. The coefficients for *s*-polarized light where the electric field is perpendicular to the plane-of-incidence are

$$r_s = \left( \frac{\mathbf{E}_{0r}}{\mathbf{E}_{0i}} \right)_s = \frac{n_i \cos \theta_i - n_t \cos \theta_t}{n_i \cos \theta_i + n_t \cos \theta_t} \quad \text{and} \quad t_s = \left( \frac{\mathbf{E}_{0t}}{\mathbf{E}_{0i}} \right)_s = \frac{2n_i \cos \theta_i}{n_i \cos \theta_i + n_t \cos \theta_t}. \quad (42)$$

For *p*-polarized light with the electric field component parallel to the plane-of-incidence

$$r_p = \left( \frac{\mathbf{E}_{0r}}{\mathbf{E}_{0i}} \right)_p = \frac{n_t \cos \theta_i - n_i \cos \theta_t}{n_i \cos \theta_t + n_t \cos \theta_i} \quad \text{and} \quad t_p = \left( \frac{\mathbf{E}_{0t}}{\mathbf{E}_{0i}} \right)_p = \frac{2n_i \cos \theta_i}{n_i \cos \theta_t + n_t \cos \theta_i}. \quad (43)$$

Above equations can be used for a single interface from one medium to another. For a slab of material there are a lot of internal reflections (see Fig 1) causing the light to encounter multiple interfaces. An incoming ray on a dielectric slab reflects and refracts. There are multiple internal reflections and at each interaction there is also light refracting out of the material. Very in-depth derivation is done in [Feenstra, 2017] by summing over all the internal reflections. This reduces to

$$\mathbf{E}_{0t} = \mathbf{E}_{0i} tt' e^{i\Delta\phi_1} \sum_{k=0}^{\infty} \left[ r'^2 e^{i\Delta\phi} \right]^k, \quad (44)$$

$$\mathbf{E}_{0r} = \mathbf{E}_{0i} r + \mathbf{E}_{0i} tt' r' e^{i\Delta\phi} \sum_{k=0}^{\infty} \left[ r'^2 e^{i\Delta\phi} \right]^k. \quad (45)$$

These equations can be simplified by using geometric series and become:

$$\mathbf{E}_{0t} = \mathbf{E}_{0i} \cdot \frac{tt' e^{i\Delta\phi_1}}{1 - r'^2 e^{i\Delta\phi}}, \quad (46)$$

$$\mathbf{E}_{0r} = \mathbf{E}_{0i} \cdot \left[ r + \frac{tt' r' e^{i\Delta\phi_1}}{1 - r'^2 e^{i\Delta\phi}} \right]. \quad (47)$$

The reflection and transmission coefficient for the full slab now becomes:

$$r_{\text{FP}} = r + \frac{tt' r' e^{i\Delta\phi_1}}{1 - r'^2 e^{i\Delta\phi}} \quad \text{and} \quad t_{\text{FP}} = \frac{tt' e^{i\Delta\phi_1}}{1 - r'^2 e^{i\Delta\phi}}, \quad (48)$$

where *t* and *r* indicate the corresponding coefficients as described in (42) and (43). The *t'* and *r'* indicate these same equations, but with the incident and transverse variables swapped (i.e. all *i* subscripts become *t*). The phase shift due to the different path lengths in the material are accounted for by  $\phi$  and  $\phi_1$ , which are:

$$\Delta\phi = \frac{4\pi d n_t}{\lambda} \cos \theta_t \quad \text{and} \quad \Delta\phi_1 = \frac{2\pi d n_t}{\lambda \cos \theta_t}. \quad (49)$$

The real reflectance and transmittance of the Fabry-Perot slab are

$$\mathcal{R} = r_{\text{FP}} r_{\text{FP}}^* \quad \text{and} \quad \mathcal{T} = t_{\text{FP}} t_{\text{FP}}^*. \quad (50)$$

## B: Derivation of Transmission Line Coefficients

In order to calculate the reflection and transmission coefficient we have to know every variable found in Figure 2. This is a summary of section 8.5 in [Goldsmith, 1998]. A few variables are already written down in Equations (9) up to (16). At first we define the input voltage  $V_{\text{gen}}$  to be:

$$V_{\text{gen}} = V_a + I_a Z_s = 1 - \rho + \frac{Z_s}{Z_l} (1 + \rho) . \quad (51)$$

The voltage at the input or output of the transmission line is half that of the generator (for a perfectly matched system). The transmission coefficient of the transmission line is:

$$t = \frac{V_b}{V_a} = \frac{V_b}{V_{\text{gen}}/2} = \frac{2V_b}{V_{\text{gen}}} . \quad (52)$$

The variable  $V_b$  is given in Equation (14) and  $V_{\text{gen}}$  above in Equation (51). This gives a new transmission coefficient of:

$$t = \frac{2 \cdot (e^{-i\phi} - \rho e^{i\phi})}{1 - \rho + (Z_s/Z_l)(1 + \rho)} . \quad (53)$$

By substitution of Equation (15) the transmission coefficient reduces to

$$t = \frac{2(1 - r)e^{-i\phi}}{1 - re^{-2i\phi} + (Z_s/Z_l)(1 + re^{-2i\phi})} = \frac{(1 - r^2)e^{-i\phi}}{1 - r^2e^{-2i\phi}} \quad (54)$$

The reflection coefficient is derived by using Equations (13) and (16). We get that

$$\frac{V_a}{I_a} = Z_a = Z_s = \frac{Z_s(1 - \rho)}{1 + \rho} . \quad (55)$$

Substituting into Equation (16) gives:

$$r = \frac{Z_s(1 + \rho) - Z_l(1 - \rho)}{Z_s(1 + \rho) + Z_l(1 - \rho)} = \frac{-2ir \sin \phi e^{-i\phi}}{1 - r^2e^{-2i\phi}} . \quad (56)$$

### C: Fabry-Perot Fits

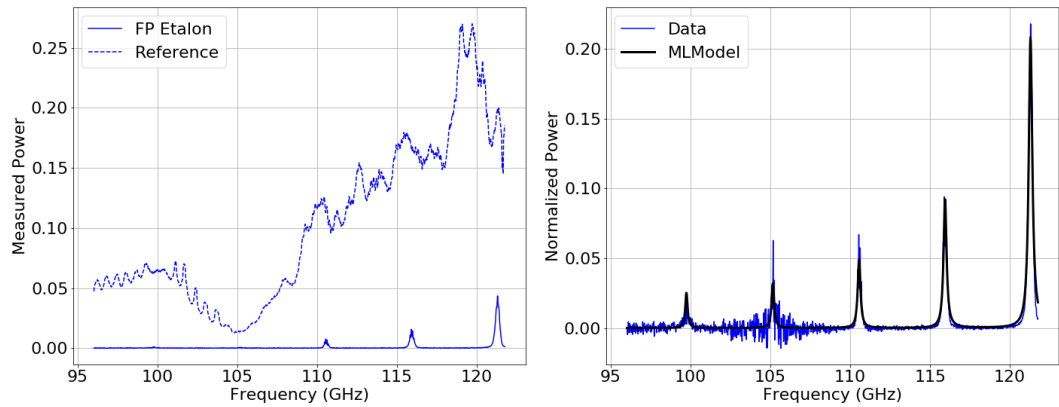


**Figure 38:** Transmission measurement of Fabry-Perot etalon with fit on full frequency range

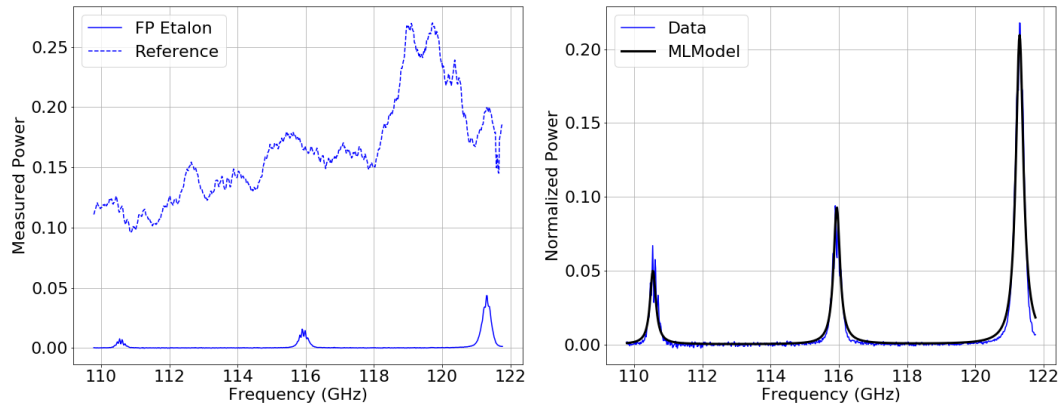


**Figure 39:** Transmission measurement of Fabry-Perot etalon with fit upward of 110 GHz

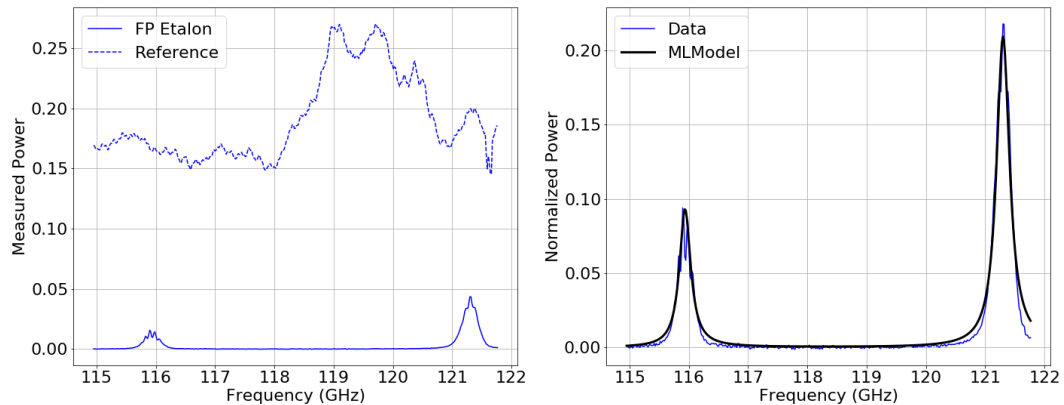


**Figure 40:** Transmission measurement of Fabry-Perot etalon with fit upward of 115 GHz

## D: Reflection Tests *s*-polarized

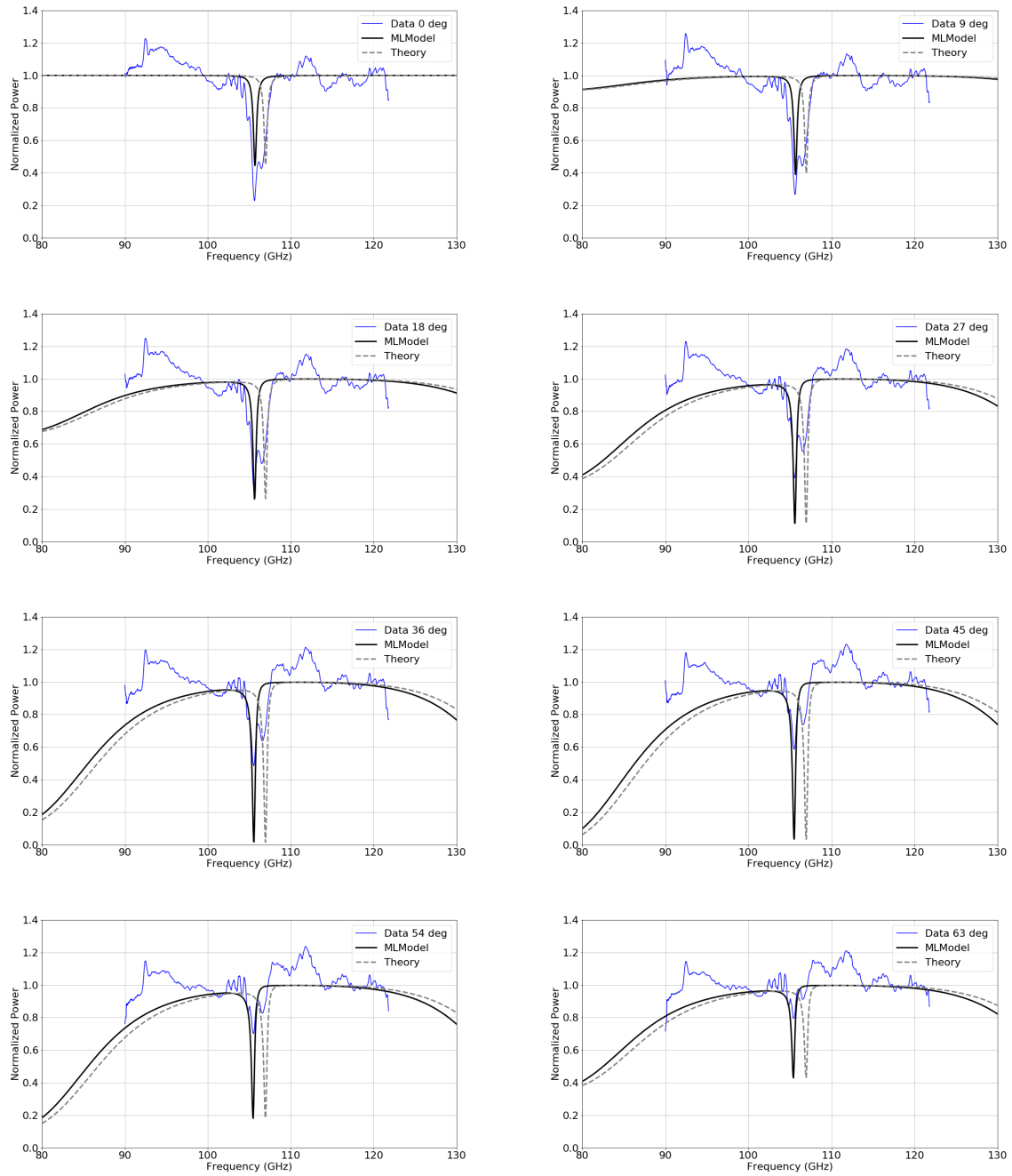


**Figure 41:** Reflectance measurements

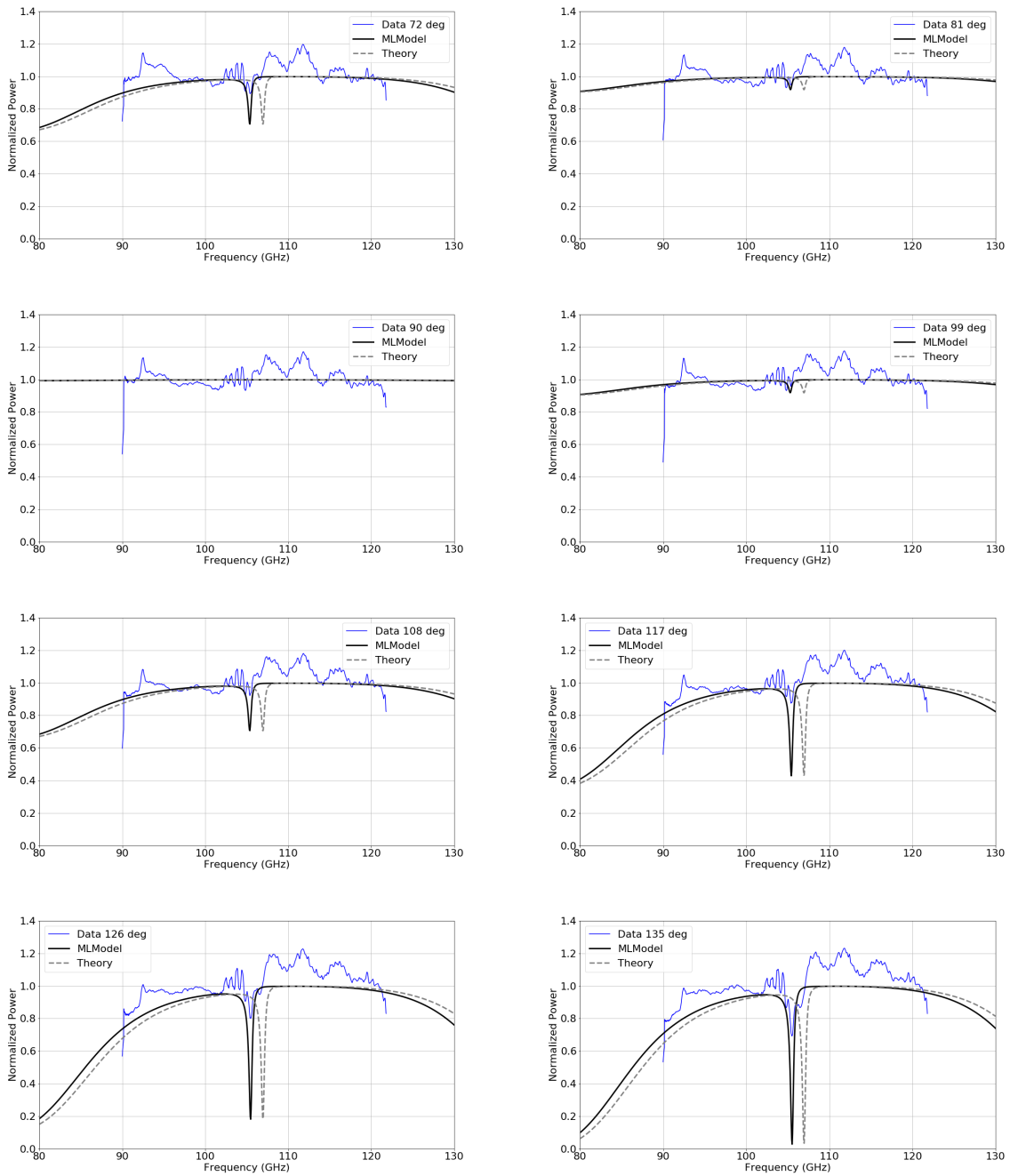


**Figure 42:** Reflectance measurements continued (1)

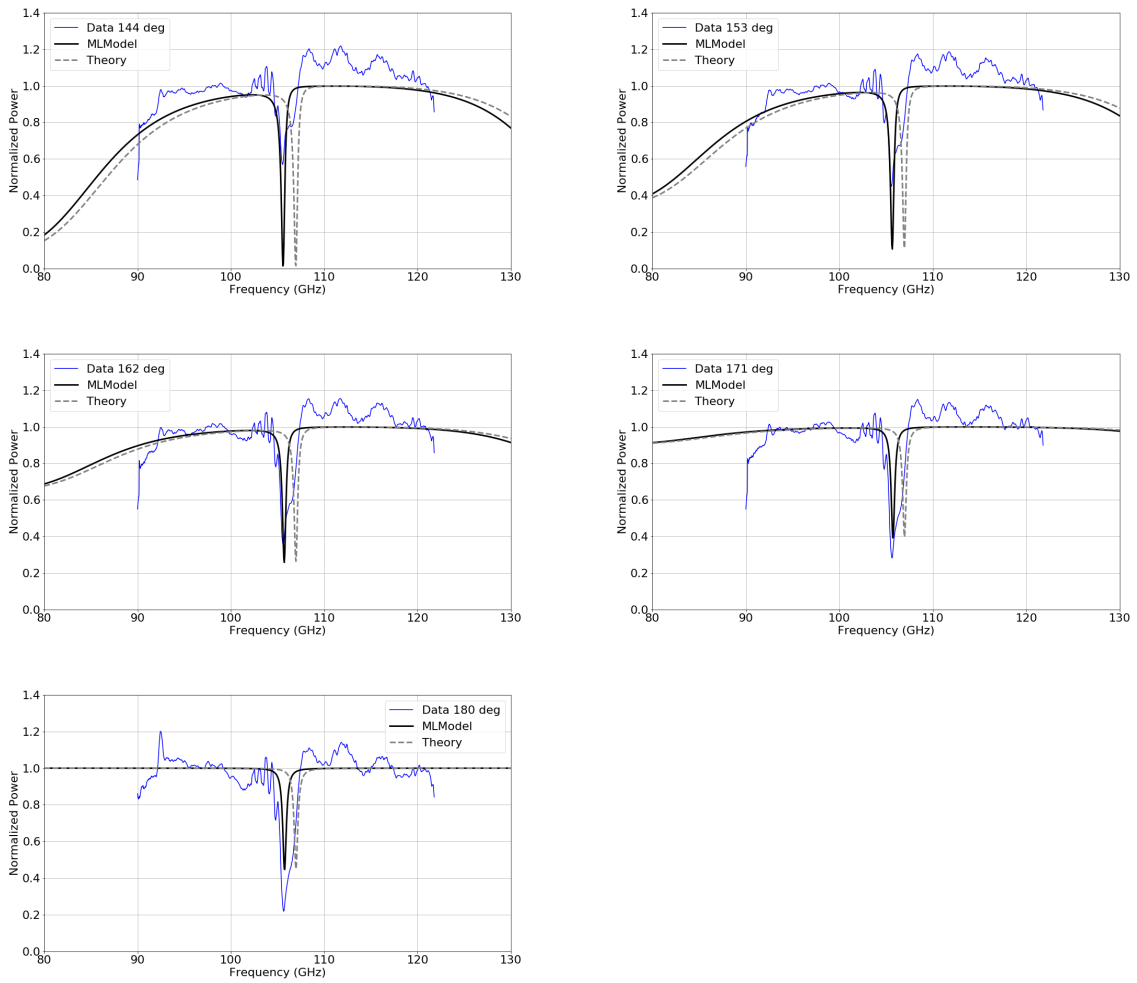


**Figure 43:** Reflectance measurements continued (2)